Mazes and meso-islands: Impact of Ag preadsorption on Ge growth on Si(111)

Th. Schmidt,[1,*] M. Speckmann,[1] J. I. Flege,[1] K. Müller-Caspary,[1] I. Heidmann,[1] A. Kubelka-Lange,[1,2] T. O. Menteş,[3] M. Á. Niño,[3,†] A. Locatelli,[3] A. Rosenauer,[1] and J. Falta[1]

[1] *Institute of Solid State Physics, University of Bremen, Otto-Hahn-Allee 1, 28 359 Bremen, Germany*

[2] *Center of Applied Space Technology and Microgravity, University of Bremen, Am Fallturm, 28 359 Bremen, Germany*

[3] *Sincrotrone Trieste, Strada Statale 14, km 163.5, 34 149 Basovizza/Trieste, Italy*

(Received 13 September 2016; published 8 December 2016)

The preadsorption of Ag on Si(111) drastically changes the growth of Ge. In a temperature range from 400 °C to 650 °C, Ag adsorption on Si leads to the formation of a $\sqrt{3}\times\sqrt{3}$-R 30° reconstruction that exhibits a maze-like morphology on the mesoscopic scale, as observed by low-energy electron diffraction (LEED) and low-energy electron microscopy. This maze morphology can be attributed to a surface roughening on an atomic scale, induced by the re-arrangement of top layer atoms during the 7×7 to $\sqrt{3}\times\sqrt{3}$-R 30° transition. The subsequent deposition of Ge results in the formation of a wetting layer, the evolution of which has been found to be governed by the Ag/Si(111)-$\sqrt{3}\times\sqrt{3}$-R 30° template's maze structure, as the latter offers a high density of heterogeneous nucleation sites. Upon further Ge growth, three-dimensional islands with diameters in the micrometer range are formed, which exhibit a large and flat (111) top facet. X-ray photoemission electron microscopy reveals that during Ge growth, Ag is segregating to the surface very efficiently. Grazing-incidence x-ray diffraction and transmission electron microscopy have been used to study the composition, strain state and defect structure of the Ge islands in dependence of the growth temperature. The strain induced by lattice mismatch is found to be largely relaxed (80–90% relaxation) in the investigated growth temperature range from 400 to 600 °C, which is confirmed by high-resolution LEED measurements. As a main relaxation mechanism, the formation of interfacial misfit dislocations has been identified. Interdiffusion of Si into the Ge islands becomes more and more pronounced for increasing growth temperature, whereas the formation of twinned Ge regions can drastically be suppressed at higher temperature.

DOI: 10.1103/PhysRevB.94.235410

I. INTRODUCTION

The growth of Ge on Si has attracted a huge interest in surface science as well as in nanotechnology. Combining Ge with Si technology provides a low-cost route to relatively fast electronic and optoelectronic devices [1–4]. From a basic research point of view, Ge growth on Si substrates is a model system for lattice mismatched heteroepitaxy. The lattice constant of Ge is 4.2% larger than that of Si, which is well known to induce a Stranski-Krastanov (SK) growth mode [5]. Except for the early growth stages [6–8], the three-dimensional (3D) SK islands typically exhibit a high defect density [9,10]. Another disadvantage of Ge growth on bare Si substrates is that the 3D island morphology associated with the SK growth mode prevents the fabrication of ultrathin Ge films, which would be useful for a wide range of applications.

One approach to solve these problems related to the SK growth mode is the so-called surfactant mediated epitaxy (SME) [11,12], where a foreign element, i.e., the surfactant (surface active agent), is preadsorbed onto the Si surface and changes the subsequent Ge growth via modification of the surface free energy [11,13] and the growth kinetics [14–20]. The surfactant reduces the surface free energy. This promotes the surface segregation of the surfactant during Ge deposition, which is a key requirement for SME.

It has been shown that group-III elements [21] and, in particular, group-V elements [11,12,16,17,20,22–32] are very well suited as surfactants for Ge growth on Si. Especially on the Si(111) surface, the preadsorption of Sb or Bi suppresses the formation of large SK islands and enables the lattice relaxation of Ge via a network of interfacial misfit dislocations [24–26]. This relaxation mechanism significantly reduces the density of stacking faults and other extended defects in the Ge film [27,28], which is reflected in charge carrier mobilities within such Ge films that are comparable to bulk Ge [33]. In addition, the interdiffusion of Si and Ge is suppressed in the case of SME [34–36], paving the road to atomically sharp interfaces.

When using group-V elements in SME, one drawback is that the incorporation of the surfactant cannot be completely suppressed, leading to an unintentional doping of the Ge films [37]. In this respect, silver might be a superior surfactant, as Ag has a significantly lower equilibrium solubility [38] in Si (1×10^{16} cm^{-3}) as compared to, e.g., Sb (5×10^{19} cm^{-3}) and Bi (8×10^{17} cm^{-3}).

Virtually all 3d, 4d, and 5d transition metals [39–43] (as well as all rare-earth metals [44–53]) form alloys and compounds with Si. The only exceptions are the rather reactive group-IIB metals [54–56] Zn, Cd, and Hg, as well as the more noble silver [57]. This has established Ag/Si as a model system for metal-on-semiconductor systems. Moreover, Ag does not alloy with Ge either [58], which makes it the most promising candidate as a surfactant for Ge/Si epitaxy among all transition metals.

While the adsorption, diffusion, and growth of Ag on Si has extensively been investigated for several decades [59–70],

*Corresponding author: tschmidt@ifp.uni-bremen.de

†Present address: Instituto Madrileño de Estudios Avanzados en Nanociencia (IMDEA-nanociencia), Campus de Cantoblanco, E–28049 Madrid, Spain.

 ©2016 American Physical Society

hardly any information about how Ag preadsorption influences the subsequent Ge growth is found in literature. The reports available so far [71,72] focus on Ge growth and surface reconstruction on partially Ag terminated Si(111), such as Ag/Si(111)-3×1. For SME, however, the surfactant surface coverage can be of crucial importance [21,71,73]. The work presented in the following, therefore, is the first study to provide a comprehensive analysis of the growth morphology, the Ge/Si intermixing, and the strain relaxation of Ge grown on completely and homogeneously Ag terminated Si(111)-$\sqrt{3}\times\sqrt{3}$-R 30° surfaces. Our study comprises results from a broad variety of complementary experimental methods, including microscopy, diffraction, and spectroscopy techniques.

II. EXPERIMENTAL

The LEED, LEEM, and XPEEM experiments discussed in the following were carried out using the SPELEEM III microscope (Elmitec GmbH) in operation at the Nanospectroscopy beamline [74] at the Elettra synchrotron laboratory, Italy. The SPELEEM combines structure sensitive low-energy electron microscopy (LEEM) with energy filtered x-ray photoemission electron microscopy (XPEEM). In the latter mode, the specimen surface is probed with soft x-ray photons, impinging on the surface at grazing incidence (16°). The emitted photoelectrons are then used for chemical imaging. The microscope reaches a lateral resolution of about 10 nm in LEEM mode and a few tens of nanometers in XPEEM mode [75,76]; in the latter mode, the best energy resolution is 0.3 eV. Apart from real-space imaging, the instrument also enables microdiffraction (μ-LEED). For this purpose, different apertures are available that confine the incident beam to the region of interest. In the present work, we probed an area of about 2 μm in diameter. Under these conditions, the SPELEEM has a transfer width of about 10 nm [76]. In addition, spot-profile analysis low-energy electron diffraction [77,78] (SPA-LEED) experiments were performed in a separate ultrahigh vacuum (UHV) setup, with a SPA-LEED instrument from Omicron GmbH. The transfer width of the SPA-LEED setup was determined to about 50 nm.

The Si(111) substrates were cut from commercially available Si wafers. After cleaning with methanol, they were introduced into the vacuum systems and degassed at about 600 °C for at least 12 hours. The sample heating was accomplished by electron bombardment of the back face of the sample in the SPELEEM and by direct current heating in the SPA-LEED setup. The temperature was monitored using infrared pyrometers and, in the SPELEEM, additionally with a WRe (type C) thermocouple spot welded onto a Mo ring supporting the sample.

The clean Si(111)-7×7 surface was prepared by flash heating up to about 1250 °C, resulting in a brilliant, low-background LEED pattern, and no contamination was visible with LEEM. Silver and germanium were evaporated from two Knudsen cells with Al_2O_3 and BN crucibles, respectively. For the experiments at the SPELEEM, Ag and Ge flux rates of 0.07 ML/min and 0.16 BL/min, respectively, were chosen, whereas the corresponding values in the experiments conducted at the SPA-LEED setup were (on average) 0.43 ML/min for Ag deposition and 0.26 BL/min for Ge growth. Here and in the following, one monolayer (ML) denotes 7.83×10^{14} atoms/cm^2, and one bilayer (BL) equals 2 ML.

The Ag evaporation rate was calibrated from the Si(111)-7×7 to $\sqrt{3}\times\sqrt{3}$-R 30° phase transition as observed by LEED, which is complete at 1 ML Ag [63]. Similarly, the Ge evaporator was calibrated from deposition of Ge on clean Si(111), which leads to a 7×7 to 5×5 transition that is complete at a coverage of 2 BL of Ge [10,79]. In the SPA-LEED setup, which was also equipped with an Sb evaporator, the latter calibration was cross-checked by Sb surfactant-mediated Ge/Si(111) growth experiments, where layer-by-layer growth occurs and LEED intensity oscillations can be observed [80].

In both UHV setups, the base pressure was below 3×10^{-10} mbar, and the pressure remained well below 1×10^{-9} mbar during Ag and Ge evaporation. In contrast to the experiments at the SPELEEM, where the Ag flux was switched off during Ge deposition, the Ag flux was kept on for Ge growth in the SPA-LEED chamber in order to compensate for Ag desorption during prolonged Ge growth at elevated temperatures. All preparation steps were monitored with LEEM, LEED, or SPA-LEED.

In comparative SPA-LEED studies without Ag co-deposition, we observed the formation of 3×1 reconstructed domains for deposition temperatures in excess of 550 °C, indicative of partial Ag desorption. As previously shown [71], Ge growth on Ag/Si(111)-3×1 leads to a different morphology as compared to Ag/Si(111)-$\sqrt{3}\times\sqrt{3}$-R 30°. In the SPELEEM experiments discussed in the following, the temperature was always below the desorption threshold.

In addition to the *in situ* LEEM, XPEEM, and SPA-LEED investigations, a sample series that had been prepared in the SPA-LEED setup was investigated *ex situ* by grazing-incidence x-ray diffraction (GIXRD) and transmission electron microscopy (TEM). The GIXRD experiments were carried out at the wiggler beamline BW2 at the storage ring DORIS at DESY, Hamburg (Germany). For this purpose, a z-axis diffractometer setup [81] and a monochromatic beam with 10.0 keV photon energy under an incident angle of 1.0° with respect to the sample surface were employed. The diffracted intensity was recorded with a one-dimensionally position sensitive detector (MYTHEN module [82]) oriented parallel to the sample surface. This allows one to acquire two-dimensional reciprocal space maps by performing one-dimensional line scans in reciprocal space.

The TEM measurements were performed at an FEI Titan G1 80/300 (S)TEM facility operated at 300 kV. The microscope is equipped with an aberration corrector for the spherical aberration of the objective lens. Conventional high-resolution TEM (HRTEM) images were recorded close to Scherzer condition, corresponding to values for the spherical aberration constant C_s ranging from 1 to 8 μm. The direction of the incident electron beam was $[1\bar{1}0]$. The specimens were prepared by mechanical grinding and subsequent ion milling at a Gatan Precision Ion Polishing system using Ar^+ ions with an energy between 3 and 4 keV. Nanobeam electron diffraction (SANBED) was performed by scanning the electron beam over the specimen in scanning TEM (STEM) mode with a semiconvergence angle of 2.3 mrad, assuring that adjacent convergent beam electron diffraction (CBED) discs did not

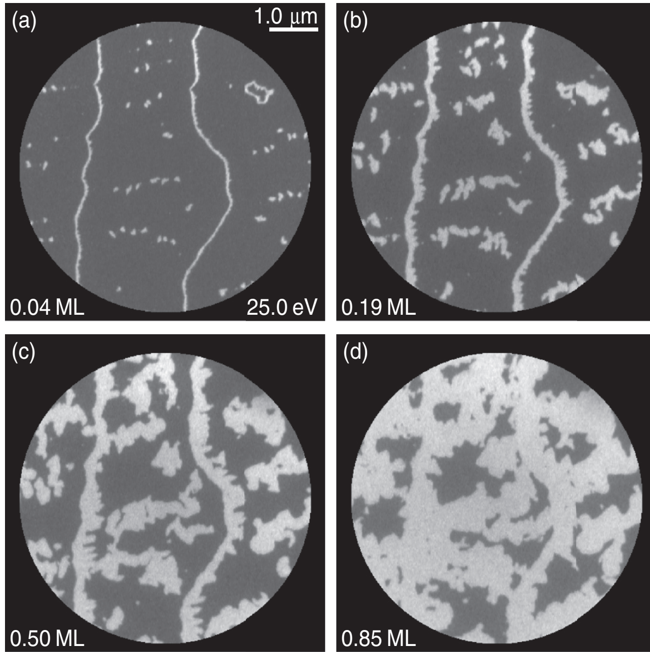

FIG. 1. Bright-field LEEM images obtained during adsorption of Ag on Si(111) at 550 °C. The Ag coverage is indicated in each frame.

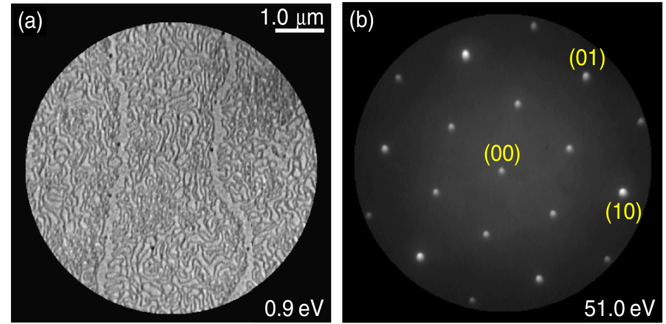

FIG. 2. (a) Bright-field LEEM image after Ag saturation of the Si(111) surface at 550 °C. The contrast leading to the "maze" pattern is most likely due to an atomic step height surface roughness. (b) LEED image (logarithmic grayscale, integer order spots indexed) obtained from the same surface, showing a single-phase $\sqrt{3}\times\sqrt{3}$-R 30° diffraction pattern, proving that the contrast in (a) does not arise from different superstructures.

overlap. For each beam position, a CBED diffraction pattern was recorded with 1 s integration time and a sampling of approximately 130 pixels per CBED disc diameter. STEM images were recorded with an annular dark-field detector (Fischione Model 3000) with acceptance angles of 33–250 mrad and with a semiconvergence angle of 9 mrad for the STEM probe.

III. RESULTS AND DISCUSSION

A. Ag preadsorption

Prior to Ge growth, a Ag/Si(111)-$\sqrt{3}\times\sqrt{3}$-R 30° surface was prepared by deposition of Ag at a substrate temperature of about 550 °C. The adsorption process is illustrated in Fig. 1. At this temperature, the Ag covered $\sqrt{3}\times\sqrt{3}$-R 30° domains (bright areas) decorate the step edges of the substrate, as can be seen in Fig. 1(a), where two step edges are within the field of view, running from the top to the bottom of the image. In addition, a few $\sqrt{3}\times\sqrt{3}$-R 30° patches nucleate on the terraces in between the step edges. As these nuclei are, in most cases, not randomly distributed over the Si(111) surface, but aligned in rows running more or less perpendicularly to the step edges, it seems most likely that this nucleation takes place at domain boundaries of the initial 7×7 structure of the bare surface [83].

The initial stage of Ag adsorption on Si(111) is very similar to the high-temperature adsorption of Ga on Si(111), which also decorates step edges and initial domain boundaries of the substrate [83]. It has been shown that, in the case of Ga adsorption, this type of decoration can be employed for selective growth of nanoscale Ge 3D islands at the step edges and domain boundaries [84]. This is different for Ag step-edge decoration, which is found to have hardly any influence on subsequent Ge growth [71].

With increasing Ag coverage, as shown in Figs. 1(b) and 1(c), the Ag terminated domains grow with an irregular and dendritic shape, and the threefold symmetry of the surface is only weakly reflected by the $\sqrt{3}\times\sqrt{3}$-R 30° domain shape. In Fig. 1(d), these domains are virtually completely coalesced, and finally the whole surface is $\sqrt{3}\times\sqrt{3}$-R 30° reconstructed, as can be seen from the LEED pattern in Fig. 2(b). A closer real-space inspection of the completely Ag terminated surface reveals a small-scale irregular pattern, as shown in Fig. 2(a), which we refer to as "maze" structure in the following. Since from the LEED pattern in Fig. 2(b) no other contributions than $\sqrt{3}\times\sqrt{3}$-R 30° can be detected, the maze pattern in real space cannot be related to the coexistence of domains with different superstructure. The contrast revealing the maze pattern is most pronounced at very low electron energies close to the mirror electron microscopy (MEM) regime and gets weaker at higher energies. Generally, MEM is sensitive to the local work function and field gradients, thus to the surface chemical composition and to the surface morphology [85]. As no evidence for chemical inhomogeneity could be observed, this finding indicates that the maze pattern is produced by surface roughness. Since we start with a smooth surface, this roughness has to be considered as a consequence of Ag adsorption. This can be understood in terms of insertion of alternating up and down step edges, as follows.

Comparing the atomic structure of the 7×7 reconstruction of the Si(111) surface as described by the dimer-adatom-stacking fault (DAS) model [86] (sketched in Fig. 3) with that of the Ag/Si(111)-$\sqrt{3}\times\sqrt{3}$-R 30° reconstruction as described by the honeycomb-chained-trimer (HCT) model [62] (shown in Fig. 4), the former consists of a complete *bilayer* of Si atoms plus a small amount of additional Si atoms, while the latter requires a *monolayer* of Si atoms in the reconstruction. Hence, about one monolayer of Si must be added (or removed) from the 7×7 reconstruction to form $\sqrt{3}\times\sqrt{3}$-R 30° domains. Starting with an ideally flat 7×7 terrace, this will lead to $\sqrt{3}\times\sqrt{3}$-R 30° domains that are one monolayer lower (type 1) than the 7×7 domains. In their vicinity, the removed Si can then be used to form $\sqrt{3}\times\sqrt{3}$-R 30° domains that are one monolayer higher (type 2) than the 7×7 surface. This scheme is

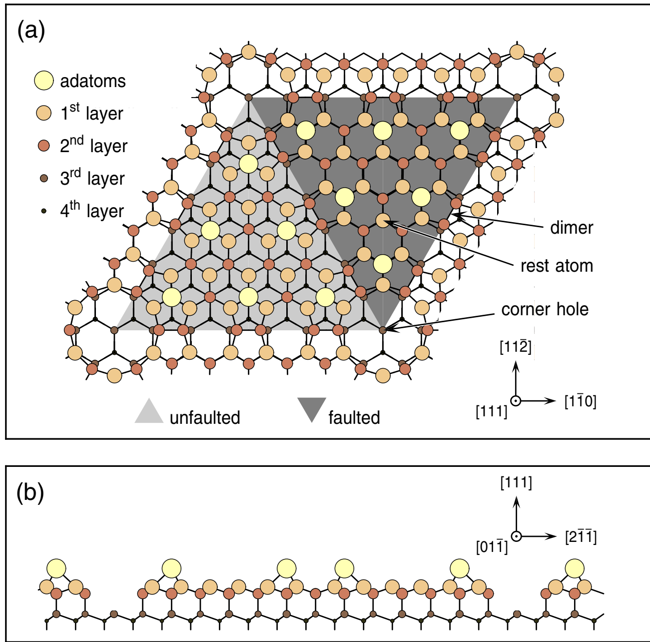

FIG. 3. (a) Top view of the Si(111)-7×7 surface according to the dimer-adatom-stacking-fault (DAS) model by Takayanagi *et al.* [86]. (b) Cross section from the lower left to the upper right corner hole of the reconstruction. Within the topmost four monolayers and including the adatoms, the 7×7 reconstruction comprises of 200 silicon atoms, as compared to 196 atoms in case of 2 bilayers of the bulk structure.

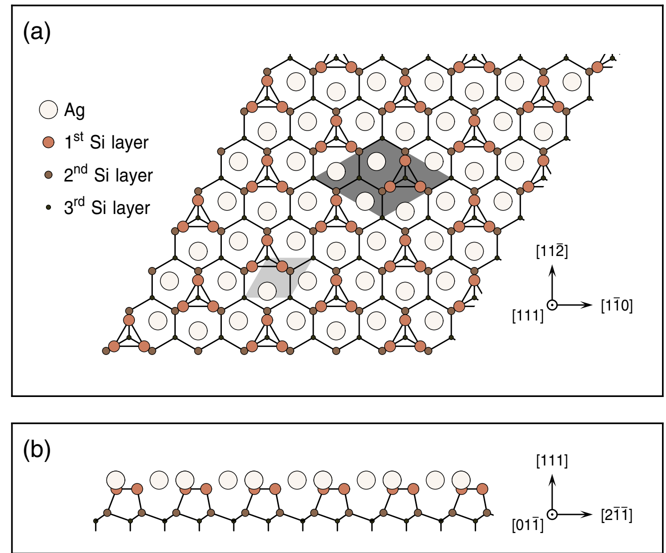

FIG. 4. (a) Top view of the Ag/Si(111)-$\sqrt{3}\times\sqrt{3}$-R 30° surface according to the honeycomb-chained-trimer (HCT) model by Ding *et al.* [62]. The small and the large shaded areas mark a 1×1 and a $\sqrt{3}\times\sqrt{3}$-R 30° unit mesh, respectively. (b) Cross section from the bottom left towards the top right of the slab shown in (a). The top bilayer of this reconstruction is a mixed bilayer and consists of one monolayer of Si and one of Ag.

in agreement with scanning tunneling microscopy results in the submonolayer coverage regime as reported by Wan *et al.* [63] and, similarly, by Voigtländer *et al.* [17] for Ga/Si(111). Once the whole terrace is $\sqrt{3}\times\sqrt{3}$-R 30° reconstructed, the type-1 and type-2 domains are separated by a substrate bilayer step. This explains the atomic arrangement forming the maze pattern, consisting of $\sqrt{3}\times\sqrt{3}$-R 30° terraces of different height, separated by Si(111) bilayer steps. As the symmetry of a flat terrace is broken at substrate step edges, also the maze pattern is disconnected there such that the position of the initial step edges remain visible, as can be seen from a comparison of Fig. 2(a) to Fig. 1(a) that shows both the same surface area except for a small drift of the specimen.

B. Ge growth on Ag/Si(111)-$\sqrt{3}\times\sqrt{3}$-R 30°

The evolution of the surface morphology during Ge deposition onto the Ag/Si(111)-$\sqrt{3}\times\sqrt{3}$-R 30° surface at 500 °C is shown in Fig. 5. Even with enhanced image contrast [cf. Fig. 5(a)], the maze pattern prior to Ge deposition is hardly visible at the electron energy of 9 eV chosen for this experiment. This is changed for submonolayer Ge deposits Θ_{Ge}, as demonstrated in Fig. 5(b), where the internal step edges of the maze structure become clearly visible. This can be attributed to a two-dimensional growth of Ge that nucleates at these steps, presumably adsorbed at the lower side of the step edge. At $\Theta_{\mathrm{Ge}} \approx 0.5$ BL, the next Ge layer nucleates at the initial step edges of the substrate [see the darkest areas in Fig. 5(c), which was recorded at a slightly higher coverage of 0.7 BL]. Only a few nuclei of this layer are found on the initial terraces between the step edges. This implies that there are hardly any heterogeneous nucleation sites such as the internal step edges of the maze structure left on the terraces, and only the initial step edges of the substrate act as preferential nucleation sites. This points to a smoothing of the surface when about half a bilayer of Ge has been deposited. This is consistent with a scheme in which the Ge fills the trenches of the maze pattern and thus confirms the interpretation of the maze pattern given above.

Interestingly, the Ge layer that has nucleated in Fig. 5(c) still mimics the maze structure, as can be deduced from the shape of the dark areas in Fig. 5(d). At first glance, this seems to contradict the smoothing of the surface at $\Theta_{\mathrm{Ge}} \approx 0.5$ BL that has been deduced above, as on a resmoothed substrate either step flow or homogeneous nucleation of 2D islands is expected. While homogeneous nucleation is observed only to a little extent even on terraces as wide as 2 microns, we find a modified step flow growth which does not proceed with a straight growth front but follows the initial maze pattern. This gives further support for the above assumption that the first Ge layer (i.e., about 0.5 BL Ge) has only filled the trenches of the maze pattern, because this implies that the terraces are smooth, but they consist of Ag/Si(111) and Ag/Ge/Si(111) patches, transforming the initial morphological maze pattern into a chemical pattern with the same topology. Our finding of a modified step-flow growth can then be explained by the fact that the layer growing on top of the chemical pattern experiences differences in surface, interface, and strain energies, depending on the local chemical composition below.

At $\Theta_{\mathrm{Ge}} = 1.6$ BL, as depicted in Fig. 5(e), the layer nucleated in Fig. 5(c) is almost complete. After that, the LEEM contrast is strongly reduced [cf. Fig. 5(f)], and virtually no change is detected on the Ge wetting layer upon further

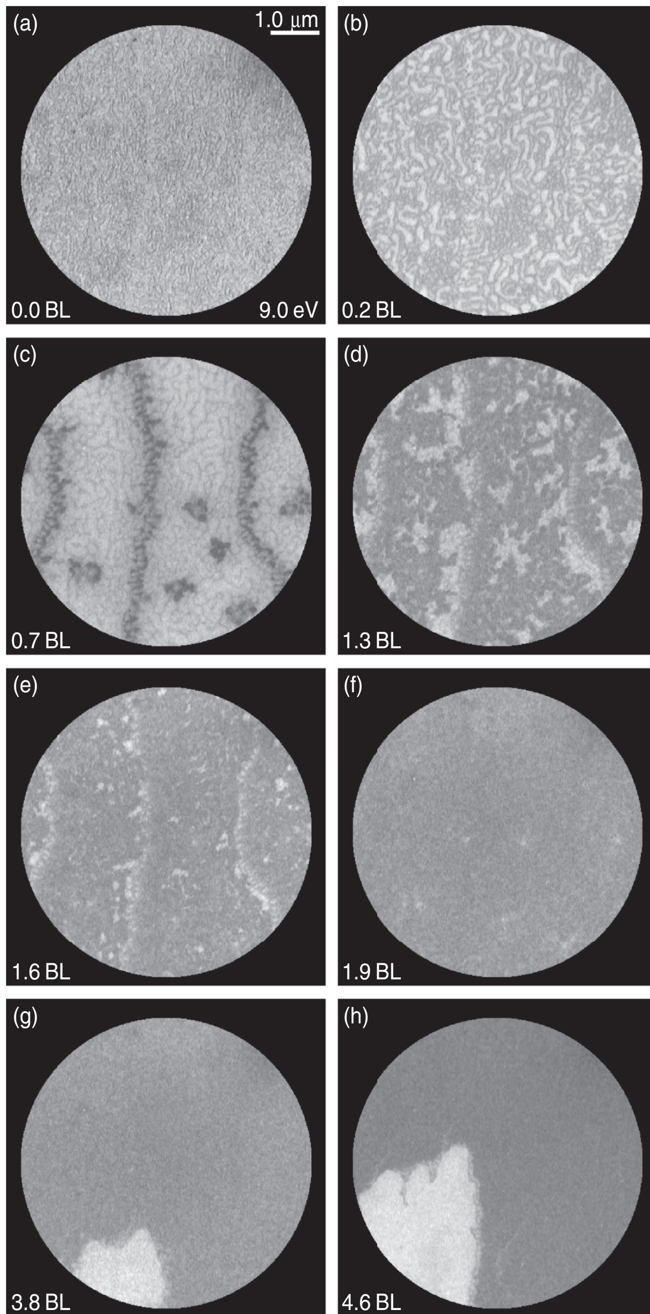

FIG. 5. Bright-field LEEM images during Ge growth on Ag/Si(111)-$\sqrt{3}\times\sqrt{3}$-R 30°at 500 °C. The Ge deposit is indicated in each frame. After the wetting layer formation (a)–(f), a large Ge island comes into the field of view in (g) and (h). Note that the contrast in frame (a) has been specially enhanced to make the initial "maze" structure better visible at this electron energy (9.0 eV). The display contrast of the images has been adjusted for each frame separately (see Fig. 6 for reference).

deposition. In Fig. 5(g), a large Ge island, which will be identified as a three-dimensional island later, appears. It has nucleated outside the field of view and slowly grows from the bottom to the top of the image, as obvious from Fig. 5(h). Due to their large size and low density (see below), the critical coverage Θ_c for the formation of such islands is difficult to determine with LEEM but is estimated to slightly above 2 BL. At the electron energy used here, the overall bright-field LEEM intensity decreases monotonically with increasing Ge deposit, up to about 2 BL (see Fig. 6), where it increases very slowly again. The latter might be attributed to a reduction of diffusing Ge adatoms as a consequence of relaxed 3D island formation, which leads to reduced diffuse scattering and, hence, to an increase in bright-field LEEM intensity [84,87], even when no such island is in the field of view.

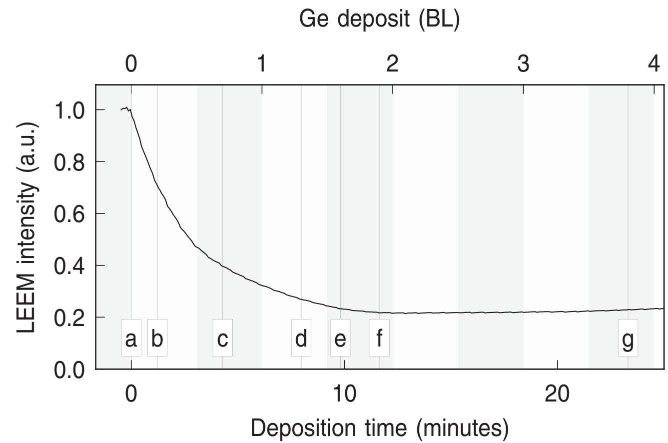

FIG. 6. Field-of-view averaged LEEM intensity for the experiment shown in Fig. 5, i.e., for bright-field LEEM at 9.0 eV, as a function of Ge deposit during Ge growth on Ag/Si(111)-$\sqrt{3}\times\sqrt{3}$-R 30° at 500 °C. The labels 'a' to 'g' refer to the image frames in Fig. 5.

C. Ge island morphology and surface chemical composition

Figure 7 shows LEEM micrographs recorded at room temperature demonstrating the surface morphology after growth of 5.2 BL Ge. A large-scale survey is presented in Fig. 7(a). At first glance, the shape of the Ge islands seems irregular,

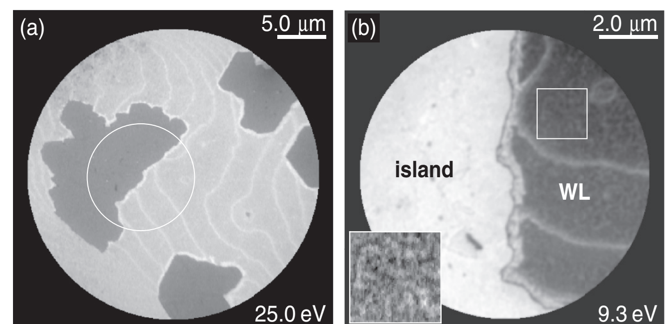

FIG. 7. Bright-field LEEM images after growth of 5.2 BL Ge on Ag/Si(111)-$\sqrt{3}\times\sqrt{3}$-R 30° at 500 °C. (a) Overview of the morphology. The Ge islands appear dark at this energy (25.0 eV). (b) Zoom into the edge of an island, marked with a white circle in frame (a). At this energy (9.3 eV), the Ge islands appear bright. The part of the wetting layer (WL) marked with a white square is shown at larger scale and with enhanced grayscale contrast in the inset at the bottom left of frame (b), in order to make the maze structure on the WL better visible. Owing to the change of magnification, the image in frame (b) is rotated with respect to the one in frame (a).

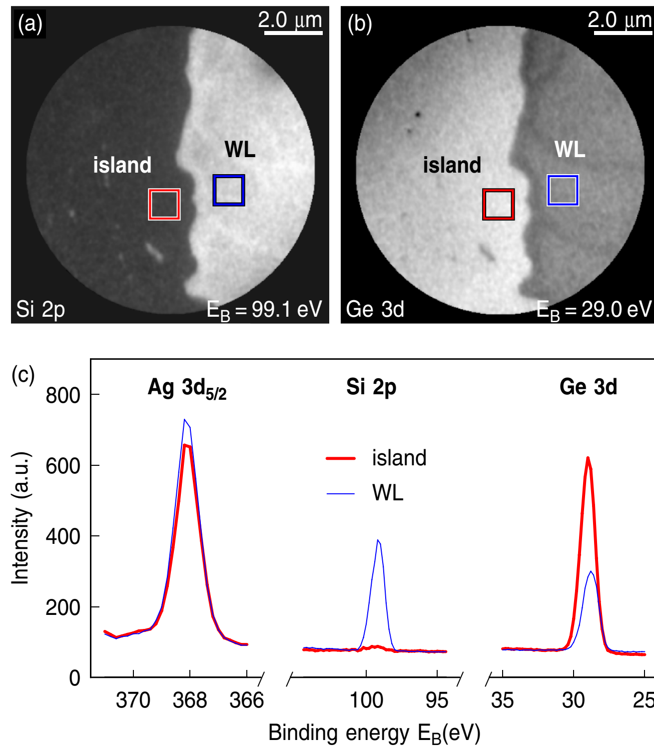

FIG. 8. XPEEM images, (a) and (b), of the same surface area as depicted in Fig. 7(b), using (a) Si $2p$ and (b) Ge $3d$ photoelectrons for imaging. The incident photon energy was 500 eV. The local spectra in (c) were obtained from XPEEM image series, integrating the intensity in the squares drawn for reference in (a) and (b).

especially when looking at the island in the left half of the image. Nevertheless, the edges of the islands tend to have preferential directions, as can be seen from the island at the right edge of the field of view in Fig. 7(a) that exposes a part of a regular hexagon.

The Ge islands are rather large with an estimated typical island diameter of up to five microns, whereas their density is extremely low, only about 5×10^5 cm^{-2}. Compared to typical island sizes and densities for germanium growth on bare silicon, our results point to a drastic increase of Ge adatom surface diffusion as a consequence of Ag preadsorption. For similar experiments using Ag as a surfactant in Si(111) homoepitaxy, Yamagami *et al.* [70] reported a very high island density and concluded on a *decreased* Si adatom mobility on Ag/Si(111)-$\sqrt{3}\times\sqrt{3}$-R 30°. However, these authors used an untypically low Si growth temperature of only 300 °C.

In Fig. 7(b), the edge of an island is depicted in more detail. Here, the wetting layer (WL) exhibits a faint maze-patterned contrast, best to be seen in the inset in Fig. 7(b). At the step edges of the wetting layer, running from left to right in the image in Fig. 7(b), as well as close to the island edge, there is clearly an increased LEEM intensity as compared to the remaining wetting layer. Such a contrast was already visible near the island edges in the growth experiment [see Figs. 5(g) and 5(h)] that was carried out at almost the same electron energy. In that experiment, the LEEM intensity of the wetting layer decreased with increasing Ge coverage (cf. Fig. 6), therefore, the bright areas on the wetting layer in Fig. 7(b) are likely to correspond to thinner regions of the wetting layer. This is corroborated by the XPEEM images in Figs. 8(a) and 8(b) recorded with Si $2p$ and Ge $3d$ photoelectrons, respectively. Whereas the regions close to the islands and close to the step edges appear slightly brighter than the remaining wetting layer in the Si $2p$ image, they appear somewhat darker in the Ge chemical image. This is explained by a thinner Ge wetting layer in these regions which diminishes the Ge $3d$ yield and increases the Si $2p$ yield because of the reduced attenuation of the Si signal originating from the buried substrate. The thinning of the wetting layer close to the island is attributed to a growth process in which the islands grow in expense of the wetting layer, i.e., the wetting layer in the vicinity of the islands becomes unstable due to the attractive chemical potential of the islands. Such an energetically favorable incorporation of Ge atoms into the 3D islands is explained by a reduction of the strain energy, since the islands show a strong lattice relaxation, as will be shown below.

When switching from Si to Ge photoelectrons, the contrast in Figs. 8(a) and 8(b) between the island and the wetting layer is inverted, clearly identifying the island to mainly consist of Ge. In the lower halves of the XPEEM images in Fig. 8, a few pits can be identified within the island, i.e., bright regions in the Si $2p$ image that appear dark in the Ge $3d$ image.

Apart from these pits, the XPEEM intensities of the Ge island are very homogeneous, and the edge of the island appears quite sharp. Micro-LEED experiments not shown here exhibit a clear $\sqrt{3}\times\sqrt{3}$-R 30° pattern on the wetting layer as well as on the islands. No LEED spots were detected that would correspond to inclined side facets of the islands, indicating that the islands are flat with a large (111) top facet. This island morphology is clearly confirmed by cross-sectional STEM, as shown in the overview image in Fig. 9, where the Ge islands appear rather like a (discontiguous) Ge film. Moreover, the $\sqrt{3}\times\sqrt{3}$-R 30° reconstruction on the Ge islands as well as on the wetting layer is an indication that the surface is still Ag terminated, i.e., that Ag has segregated to the surface during growth, since also for Ag/Ge(111) the high-coverage phase is a $\sqrt{3}\times\sqrt{3}$-R 30° HCT reconstruction [88] (and no Ag was co-deposited during Ge growth). The surface segregation of Ag in case of Ge epitaxy on Si(111) is corroborated by quantitative XPEEM and SPA-LEED analyses, as detailed below. We note that surface segregation of Ag has also been demonstrated in the case of Si(111) homoepitaxy [70].

In Fig. 8(c), local XPEEM spectra obtained from a region on an island and from an area on the wetting layer are compared.

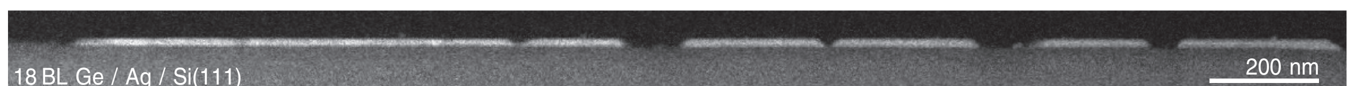

FIG. 9. Cross-sectional HAADF-STEM image of Ge islands (bright) grown at 550 °C on Ag/Si(111)-$\sqrt{3}\times\sqrt{3}$-R 30°. The Ge deposit is 18 BL.

As expected for Ge 3D islands, the Ge $3d$ signal is much larger on the island as opposed to the wetting layer. Owing to a limited inelastic mean free path length (IMFP) of the photoelectrons, however, the ratio of the Ge $3d$ intensities $I_{\rm isl}/I_{\rm WL}$ does not directly reflect the thickness ratio $d_{\rm isl}/d_{\rm WL}$ of island and wetting layer. More precisely, the intensity ratio can be expressed as

$$r_{\rm Ge} = \frac{I(d_{\rm isl})}{I(d_{\rm WL})} = \frac{1 - e^{d_{\rm isl}/\Lambda}}{1 - e^{d_{\rm WL}/\Lambda}},$$

which in the case of a thick island ($d_{\rm isl} \gg \Lambda$) leads to

$$d_{\rm WL} = \Lambda \log\left(\frac{r_{\rm Ge}}{r_{\rm Ge} - 1}\right).$$

Here, Λ is an effective attenuation length with contributions Λ_e from electron attenuation (under normal emission) and Λ_p from photon attenuation (under grazing angle α):

$$\frac{1}{\Lambda} = \frac{1}{\Lambda_e} + \frac{1}{\Lambda_p \sin(\alpha)}.$$

In the present case, Λ can be approximated by the IMFP for Ge $3d$ photoelectrons with a kinetic energy of 471 eV, which amounts [89] to $\Lambda_e = 12.5$ Å, whereas the contribution from photon attenuation at 500 eV photon energy [90], $\Lambda_p = 2120$ Å, is negligible, even for an incident angle of $\alpha = 16^\circ$. Using these values, and $r_{\rm Ge} = 2.3$ as determined from the data in Fig. 8, we obtain $d_{\rm WL} = 7.1$ Å. This corresponds to a Ge coverage of 2.2 BL, in good agreement with the critical coverage for 3D island formation as estimated from the growth experiment at the end of Sec. III B above.

The attenuation due to a finite IMFP can well be seen in the local Si $2p$ spectra. Compared to the Si signal from the wetting layer, the yield from the island is almost negligible. The very small Si $2p$ peak detected on the island could either originate from the substrate if the islands are rather thin, or, in the case of thick islands, it originates from Si incorporated into the Ge islands. In the latter case, assuming homogeneous Ge/Si intermixing, the Si concentration $c_{\rm Si}$ in the islands can be calculated. According to Ratto *et al.* [91,92],

$$c_{\rm Si} = \frac{r_{\rm Ge} - 1}{r_{\rm Ge}/r_{\rm Si} - 1}, \qquad (1)$$

where $r_{\rm Ge}$ and $r_{\rm Si}$ are the ratios of the integrated photoelectron peak intensities $I_{\rm isl}/I_{\rm WL}$ on the island and on the wetting layer, for Ge $3d$ and Si $2p$, respectively. In the present case, $r_{\rm Ge} = 2.3$ and $r_{\rm Si} = 0.057$, thus a maximum silicon concentration of about $(3 \pm 0.5)\%$ is deduced. This is quite a low value, as compared to Ge islands grown on bare Si surfaces (not shown here), for which a value of $c_{\rm Si} = 0.18$ is obtained at the same growth temperature of 500 °C, using the same analytical model [Eq. (1)]. This result suggests that, with Ag preadsorption, virtually no intermixing between Ge and Si takes place at this growth temperature and that an atomically sharp interface between Ge and Si might be achieved. It should be noted, however, that this approach to determine the Si concentration cannot take into account a gradient of the Si concentration. Therefore, the island parts closer to the interface might contain more Si than the value determined here. From *ex situ* investigations presented in Sec. III E, the latter scenario is corroborated.

No element-sensitive image using Ag photoelectrons has been shown in Fig. 8, as there is almost no contrast to be seen. This is reflected by the almost equal peak height of the Ag $3d_{5/2}$ signal on the island and on the wetting layer, as shown on the left-hand side of Fig. 8(c). The almost equal intensity implies that the Ag has not been buried by the Ge deposited on top, because otherwise, a ratio similar to that for the Si $2p$ signal would have been observed (with an even more efficient suppression of the Ag $3d_{5/2}$ emission line due to the lower kinetic energy, which in this range is associated with a shorter IMFP [89]). Clearly, this is not the case. Keeping in mind that the Ag flux was turned off during Ge deposition, the XPEEM data shows that Ag segregates to the surface. Moreover, the segregation is very efficient because only a very small difference is found in the Ag surface coverage for the island and for the wetting layer. From the data shown in Fig. 8(c), a ratio of $r_{\rm Ag} = 0.87 \pm 0.08$ is determined for the Ag $3d_{5/2}$ intensity on the islands and on the wetting layer. (Similar to the Ge and Si signals, the relative uncertainty of $\Delta r_{\rm Ag}/r_{\rm Ag} \approx 10\%$ arises mainly from inhomogeneities of the illumination.) Such a value less than unity can be explained (i) by incorporation of Ag into Ge, (ii) by thermal desorption of Ag (which would have to be more efficient from islands than from the wetting layer in that case), or (iii) by strain relaxation (as will be explained below). Though Ag incorporation or desorption cannot be completely ruled out, they seem unlikely to be the main reason for a reduced Ag photoelectron yield on the islands, because incorporation as well as desorption alone would lead to a lack of Ag in the $\sqrt{3}\times\sqrt{3}$-R 30° reconstruction. For a reduction of roughly 10%, as detected here, one could expect that other surface reconstructions with a lower Ag coverage form and coexist with $\sqrt{3}\times\sqrt{3}$-R 30°, such as [63,71,72] 3×1, or even 5×5 or 7×7. As mentioned above, this can be ruled out from μ-LEED experiments.

Whereas no indication for Ag incorporation or desorption can be found from the LEED patterns, LEED provides evidence for lattice relaxation. Figure 10 shows SPA-LEED data obtained prior to Ag adsorption and after Ge growth on Ag:Si(111)-$\sqrt{3}\times\sqrt{3}$-R 30°. The pattern in Fig. 10(b) shows that the surface is $\sqrt{3}\times\sqrt{3}$-R 30°-reconstructed after Ge growth. Remarkably, all diffraction spots, except for the (00) spot, are split. For the integer spots, a comparison to the initial 7×7 pattern in Fig. 10(a) reveals that the additional spots appear at positions somewhat closer to the (00) spot. This indicates an additional surface phase with a slightly larger in-plane lattice constant, which can be attributed to a partial lattice relaxation of the Ge 3D islands. The degree of relaxation can be seen from Fig. 10(c), where a high-resolution radial line scan along the (01) direction is displayed. The splitting of the first order integer spot is demonstrated to be $(2.7 \pm 0.1)\%$ of the surface Brillouin zone (SBZ), corresponding to Ge with a lateral lattice constant $1/(1 - 0.027) = 1.028$ times larger than that of silicon. Thus, at least $(66 \pm 3)\%$ of the 4.2% lattice mismatch between Ge and Si have been relaxed in the flat Ge islands; the degree of relaxation might be even higher if Ge/Si intermixing is taken into account. At this growth stage and for this growth temperature, such a high degree of relaxation is comparable to Ge films grown using Sb or Bi as a surfactant [27,28]. It should be kept in mind, however,

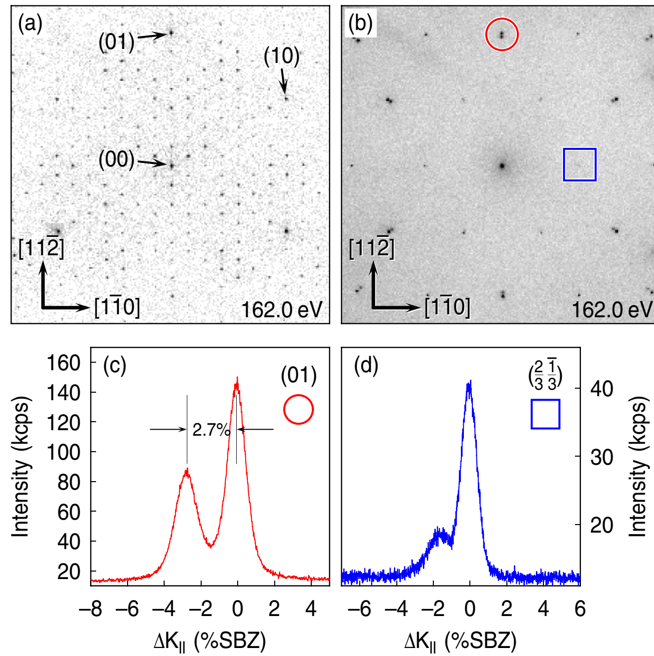

FIG. 10. SPA-LEED patterns (inverse logarithmic grayscale) (a) from a clean Si(111)-7×7 surface, and (b) after growth of about 18 BL Ge on Ag:Si(111)-$\sqrt{3}\times\sqrt{3}$-R 30° at 500 °C. Integer order spots are indexed in (a). Note the splitting of the spots in (b), best to be seen near the corners of the viewgraph. Line scans (c) and (d) were taken through (c) an integer order spot and (d) a third order spot, marked by a circle and a square in (b), respectively.

that LEED probes only a few atomic layers at the top of the islands, and other methods like x-ray and transmission electron microscopy are necessary for complete strain state and compositional analyses (see Sec. III E).

In the line scan in Fig. 10(d), which was taken at a third order reflection, also a split spot is resolved. While the reduced *absolute* splitting is easily explained by the smaller distance of that (2/3 $\bar{1}$/3) reflection with respect to the (00) spot, the presence of a relaxed component at this superstructure spot [with the same *relative* splitting as observed for the (01) spot in Fig. 10(c)] proves that the relaxed Ge islands, similar to the wetting layer, also have a $\sqrt{3}\times\sqrt{3}$-R 30° reconstruction, consistent with μ-LEED measurements as mentioned above. Returning to the XPEEM results, the lattice relaxation detected with LEED can explain a slightly decreased Ag $3d_{5/2}$ intensity on the Ge islands as compared to the wetting layer. Owing to the lattice relaxation, the Ge islands have a larger surface unit mesh than the wetting layer, whereas the surface reconstruction and, thus, the number of Ag atoms per unit mesh remains constant. From these considerations, it follows that the density of Ag atoms on the islands is $(5.6 \pm 0.3)\%$ less than on the wetting layer, in reasonable agreement with the XPEEM result of $(13 \pm 8)\%$.

D. Island coalescence and film growth

Figure 11(a) depicts the surface morphology for a Ge deposit of $\Theta_{\mathrm{Ge}} = 20.7$ BL. At this growth stage, a partial coalescence of the islands has occurred. On top of the

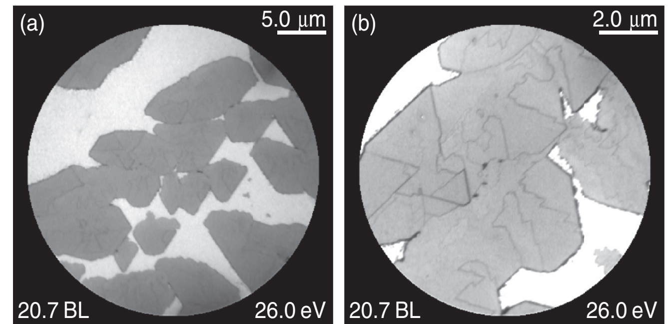

FIG. 11. Bright-field LEEM images after Ge growth at 480 °C on Ag/Si(111)-$\sqrt{3}\times\sqrt{3}$-R 30°, with a Ge deposit of 20.7 BL. The image in frame (b) is displayed at increased grayscale contrast.

islands, dark lines are visible, better discernible in the higher-magnification image in Fig. 11(b) that is reproduced with an increased grayscale contrast. These lines are preferentially running along directions that can be attributed to the threefold symmetry of the surface. At present, it is not clear whether these lines correspond to step edges or step bunches on the islands' top facets or whether they indicate grain boundaries or other extended defects. From the result to be discussed in Sec. III E, however, it seems most likely that these lines are boundaries between regular ("A-stacked") Ge and twinned ("B-stacked") Ge, as already reported for Ga mediated Ge/Si(111) epitaxy [21].

The island coalescence observed in Fig. 11 suggests that the whole surface will be covered by a Ge film upon prolonged deposition. This has been investigated in more detail by means of SPA-LEED, as shown in Fig. 12(a). During Ge deposition at 440 °C, diffraction profiles similar to the one shown in Fig. 10(c) were recorded at the Si(10) reflection at 80 eV electron energy. At the beginning of the deposition,

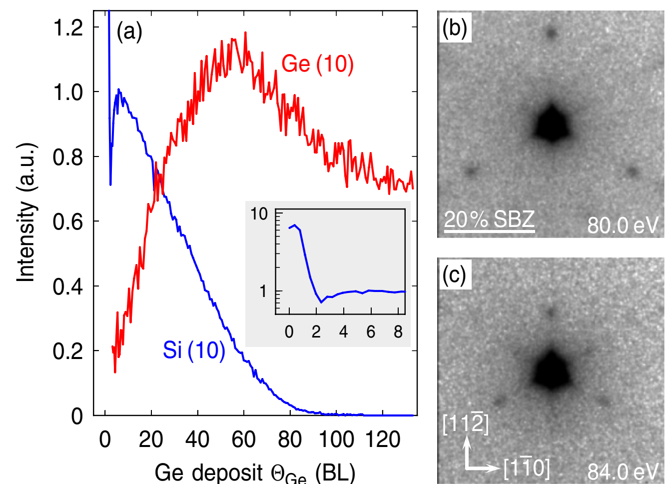

FIG. 12. (a) Evolution of the integral intensity of the Si(10) and the Ge(10) LEED spots at 80 eV during Ge deposition on Ag/Si(111)-$\sqrt{3}\times\sqrt{3}$-R 30° at 440 °C. Both curves have been scaled differently for display reasons. The inset shows the details of the Si(10) intensity evolution in the initial stage, on logarithmic scale. Frames (b) and (c) show the LEED pattern after growth in the vicinity of the (00) spot at 80 eV and 84 eV, respectively.

there is only one spot at 100% SBZ that is associated with the bare Si surface or the pseudomorphically strained Ge wetting layer. Its integral intensity in dependence of the total Ge deposit Θ_{Ge} is shown in the curve labeled "Si(10)" in Fig. 12(a). At the initial stage, the Si(10) intensity drops very rapidly, which we mainly attribute to a change of the form factor [78] upon Ge wetting layer formation. An additional contribution to the initial intensity decrease might originate from a high density of diffusing Ge adatoms, which lead to diffuse scattering [84,87] and, therefore, to a reduction of the Si(10) intensity. From $\Theta_{Ge} = 0$ to the pronounced minimum at $\Theta_{Ge} = (2.35 \pm 0.25)$ BL the Si(10) intensity is diminished by a factor of about 10. The dip at $\Theta_{Ge} = 2.35$ BL indicates the onset of Ge island formation, as can be deduced as follows.

Firstly, for $\Theta_{Ge} > 2.35$ BL, a second peak can be resolved in the diffraction profiles at $|K_{\parallel}| < 100\%$ SBZ, similar to Fig. 10(c). As explained above, this spot is attributed to partially relaxed Ge islands. The integral intensity of this spot is depicted in the curve labeled "Ge(10)" in Fig. 12(a). It shows a strong increase up to $\Theta_{Ge} \approx 55$ BL, indicating that the surface is progressively covered with Ge islands. Secondly, as shown in the discussion of the LEEM and XPEEM data above, the wetting layer becomes locally slightly thinner after Ge island nucleation. In regard of the strong decrease of the Si(10) intensity by one order of magnitude at $\Theta_{Ge} < 2.35$ BL [cf. inset in Fig. 12(a)], a slight increase as observed for $\Theta_{Ge} > 2.35$ BL is in agreement with a very local thinning of the wetting layer in the vicinity of Ge islands. Thirdly, the density of diffusing Ge adatoms can be expected to be reduced in the presence of relaxed Ge islands, which offer energetically more favorable incorporation sites than a strained wetting layer. This might also contribute to the increase of the Si(10) intensity from the wetting layer after the onset of Ge island formation [84,87]. For these three reasons it is concluded that the critical coverage for island formation is around $\Theta_{Ge} \approx 2.35$ BL.

For coverages beyond the island nucleation threshold, the Si(10) intensity increase, that is attributed to wetting layer thinning and adatom condensation, competes with the Si(10) intensity decrease due to Ge island growth. Since the Ge islands exhibit a different lattice parameter and extend over an increasing fraction of the surface area, as evidenced by the "Ge(10)" curve, the fraction of the surface that contributes to the Si(10) spot is reduced. This effect becomes dominant for $\Theta_{Ge} > 6$ BL, where the Si(10) intensity decreases monotonically. Over a wide range, the decay is linear, which points to a pronounced lateral growth of the islands while the average thickness does not change much. The intensity vanishes completely at a Ge deposit of around 90 BL, which indicates that at this coverage a continuous, relaxed Ge film has formed under the present growth conditions. In turn, one would expect the Ge(10) intensity to increase up to $\Theta_{Ge} \approx 90$ BL. However, it saturates already at about 55 BL and even decreases for still higher Ge deposits. Though a long-term drift of the emission current of the electron gun of the SPA-LEED instrument cannot be completely ruled out as an explanation, it seems more likely that defect formation and/or surface roughness on the Ge islands is the reason for the unexpectedly low Ge(10) intensity at higher coverages. Some evidence for surface roughness can be found from the diffraction patterns in Figs. 12(b) and 12(c). Here, additional spots appear in the vicinity of the (00) reflection which move when the electron energy is changed. Hence, these spots are identified as facet spots. No such facet spots could be detected, e.g., for the sample shown in Fig. 10, i.e., at a rather early stage of growth. Though the facet formation observed after prolonged growth is presently not completely understood, a possible explanation could be that it is driven by the residual strain in the Ge island layer.

E. Strain state, defects, and chemical composition

For a more detailed compositional and strain state analysis, a series of samples was investigated by means of GIXRD and TEM. The Ge growth temperature T_G was varied from 400 °C to 600 °C. The initial Ag adsorption was performed at T_G as well. The total Ge deposit of about 18 BL was kept constant throughout the sample series. Ag co-deposition was applied during Ge growth in order to prevent Ag desorption at more elevated T_G.

In Fig. 13, reciprocal space maps (RSMs) in a plane parallel to the surface (i.e., a $Q_{\parallel}$ plane), recorded in the vicinity of the $(\bar{2}\bar{2}4)$ Bragg reflection are shown for different T_G. As can be seen from Fig. 14, this Bragg reflection is located on the $(\bar{3}0)$ crystal truncation rod (CTR) at $l = 0$, i.e., it has a vanishing scattering component $Q_{\perp}$ perpendicular to the surface. Therefore, the bright spot at $h = -3$ in the RSMs shown in Figs. 13(a)–13(c) does not represent the Si$(22\bar{4})$ Bragg reflection but rather the intersection of the Si$(\bar{3}0)$ CTR with the plane of the RSM which was taken at $l \approx 0.07$. The elongated shape of the Si$(\bar{3}0)$ CTR in the RSMs in Figs. 13(a)–13(c) is caused by the rather large footprint of the beam on the sample and can therefore be considered as an instrumental broadening. At smaller absolute values of h, another bright spot occurs that is identified as the Ge$(\bar{3}0)$ CTR. For $T_G = 400$ °C, it is found at $h \approx -2.90$. Besides the two prominent CTRs, rather weak spots can be recognized that are arranged on a hexagonal grid and have been marked with black dots in Fig. 13(a). Such an array of satellite spots is typical of periodic lattice distortions induced by an ordered hexagonal network of interfacial misfit dislocations [25,26,93], as has been demonstrated in earlier GIXRD studies for Ge films grown by Sb or Bi surfactant mediated epitaxy (SME) [27,28].

At $T_G = 500$ °C, the Ge$(\bar{3}0)$ CTR becomes narrower and shifts slightly towards the Si$(\bar{3}0)$ CTR, while the array of satellite spots is still clearly visible [cf. Fig. 13(b)]. For a growth temperature of 600 °C, as shown in Fig. 13(c), the Ge CTR is still further shifted towards the Si CTR. Satellite spots, however, can hardly be identified for $T_G = 600$ °C.

From the position of the Ge spot in $Q_{\parallel}$ direction (h direction in Fig. 13), the lateral reciprocal lattice parameter $a^*_{\parallel,Ge}$ can directly be determined. Figure 13(d) shows $a^*_{\parallel,Ge}$ as determined from GIXRD in dependence of the growth temperature. As already seen qualitatively from the visual inspection of the RSMs in Figs. 13(a)–13(c), there is a monotonic increase of $a^*_{\parallel,Ge}$ in the temperature range investigated here. For comparison, according SPA-LEED results from the same sample series are superimposed in Fig. 13(d). Obviously, within the experimental uncertainty, there is a very good agreement between the GIXRD and the SPA-LEED data. Since SPA-LEED only probes the few uppermost atomic

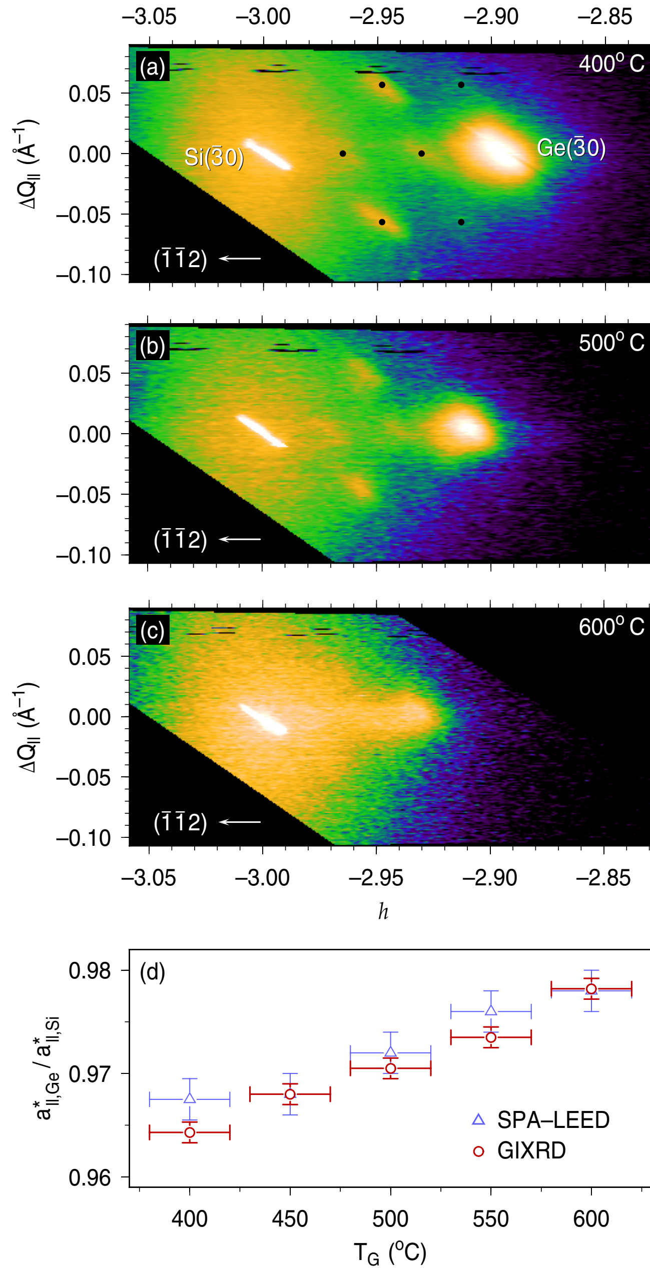

FIG. 13. Reciprocal space maps in a $Q_\parallel$ plane in the vicinity of the ($\bar{2}\bar{2}4$) reflection [i.e., near the ($\bar{3}$0)-CTR] at $l \approx 0.07$, for Ge islands grown on Ag/Si(111)-$\sqrt{3}\times\sqrt{3}$-R 30°at (a) 400 °C, (b) 500 °C, and (c) 600 °C. Satellite spots are indicated with small black dots in (a). In frame (d), the temperature dependence of the lateral reciprocal lattice parameter $a^*_{\parallel,\mathrm{Ge}}$ of the Ge islands is shown (in units of the Si bulk value $a^*_{\parallel,\mathrm{Si}}$), as determined from GIXRD (○) and SPA-LEED (△).

layers, whereas GIXRD averages over the whole volume of the islands, this agreement implies that the Ge lattice constant is quite homogeneous across the islands' height. This points to a strain relaxation mechanism that acts at the Ge/Si interface and, therefore, provides further support for the presence of an interfacial misfit dislocation network.

The increase of $a^*_{\parallel,\mathrm{Ge}}$ shown in Fig. 13(d) could, at first glance, be interpreted by a corresponding increase in strain, as has been argued for Sb SME of Ge/Si(111) [28]. In

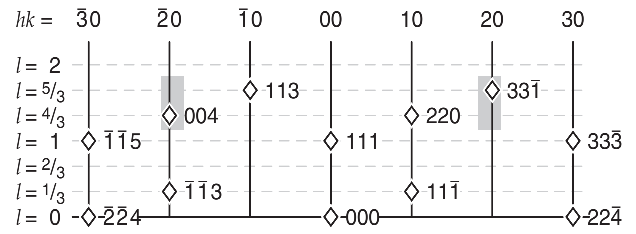

FIG. 14. Schematic of the reciprocal space of the Si(111) surface in the (111)-(11$\bar{2}$) plane. h, k, and l refer to LEED coordinates.

that case, $a^*_{\parallel,\mathrm{Ge}}/a^*_{\parallel,\mathrm{Si}}$ was reported to increase from 0.966 to 0.970 in the temperature range from 465 °C to 635 °C. This has been explained in terms of a reduction of the strain energy $w = \langle\varepsilon\rangle^2 + \sigma_\varepsilon^2$ despite an increased average strain $\langle\varepsilon\rangle$. This has been shown to be possible if, as $\langle\varepsilon\rangle$ increases, the disorder of the misfit dislocation (MD) network and, thus, the standard deviation of the strain distribution σ_ε is strongly suppressed [28]. The transition from a disordered to an ordered MD network in the case of Sb SME was concluded on from the fact that the satellite spots were diffuse and hardly visible for $T_\mathrm{G} < 500$ °C and became sharper and more intense at higher temperatures. In the present case of Ge growth on Ag terminated Si(111), such a transition cannot be identified from the data shown in Figs. 13(a)–13(c), since satellite spots can clearly be resolved already at 400 °C. Moreover, the increase of $a^*_{\parallel,\mathrm{Ge}}$ shown in Fig. 13(d) is much larger than in the case of Sb SME. Hence, the development of $a^*_{\parallel,\mathrm{Ge}}$ cannot be explained in terms of strain alone, but Ge/Si intermixing has also to be taken into account.

The intermixing of Ge and Si is corroborated by the analysis of the average vertical lattice parameters, which have been determined from $Q_\parallel$-$Q_\perp$ RSMs recorded along the Ge(20) CTR, such as the ones shown in Figs. 15(a) and 15(b) for $T_\mathrm{G} = 400$ °C and $T_\mathrm{G} = 550$ °C, respectively. Here, a tail of the Si(33$\bar{1}$) reflection, which is not located exactly in the planes represented by the RSMs, appears at l=5/3 (cf. Fig. 14). The Ge(33$\bar{1}$) Bragg spot appears at l=1.596 for $T_\mathrm{G} = 400$ °C and at slightly higher l for $T_\mathrm{G} = 550$ °C. An additional peak shows up for both temperatures at $l \approx 1.3$, which is related to twinned regions within the Ge islands, as will be discussed below. The dependence of the vertical reciprocal lattice parameter $a^*_{\perp,\mathrm{Ge}}$ on the growth temperature is shown in Fig. 15(c). Obviously, it increases with increasing T_G. Hence, with increasing temperature both the lateral and the vertical lattice parameter of the Ge islands shift towards the Si bulk value. This can only be explained by progressive Ge/Si intermixing. If the islands consisted of pure Ge for all growth temperatures, then an increase in $a^*_{\parallel,\mathrm{Ge}}$ should, as an elastic response, be accompanied by a decrease of $a^*_{\perp,\mathrm{Ge}}$ and vice versa.

Using elasticity theory, the strain state and composition can be quantitatively determined from the observed lateral and vertical lattice parameters, if Vegard's law is assumed for the bulk lattice parameter $a^\mathrm{bulk}(x)$ of a $\mathrm{Ge}_x\mathrm{Si}_{1-x}$ alloy:

$$a^\mathrm{bulk}(x) = a^\mathrm{bulk}_\mathrm{Ge}\cdot x + a^\mathrm{bulk}_\mathrm{Si}\cdot(1-x)\,, \qquad (2)$$

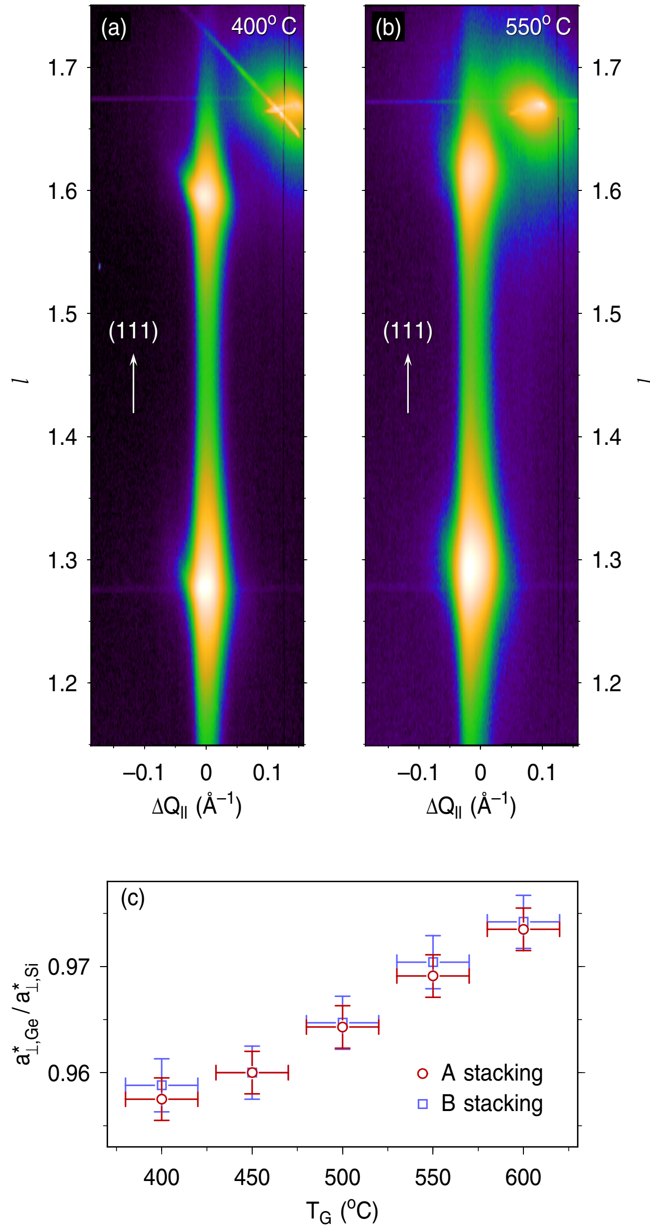

FIG. 15. Reciprocal space maps in a $Q_\parallel$-$Q_\perp$ plane, recorded on the Ge(20) CTR, for Ge islands grown on Ag/Si(111)-$\sqrt{3}\times\sqrt{3}$-R 30° at (a) 400 °C and (b) 550 °C. In frame (c), the temperature dependence of the vertical reciprocal lattice parameter $a^*_{\perp,\mathrm{Ge}}$ of the Ge islands is shown (in units of the Si bulk value $a^*_{\perp,\mathrm{Si}}$) for both regular Ge (○) and twinned Ge (□).

as well as a similar linear relationship for the elastic compliances:

$$c_{ij}(x) = c_{ij,\mathrm{Ge}} \cdot x + c_{ij,\mathrm{Si}} \cdot (1-x)\,. \quad (3)$$

After transforming the strain tensor into the (111) reference frame, the vertical strain component, and accordingly the vertical lattice parameter $a_\perp$, can be calculated for a given lateral lattice parameter $a_\parallel$ in dependence of the Ge content x

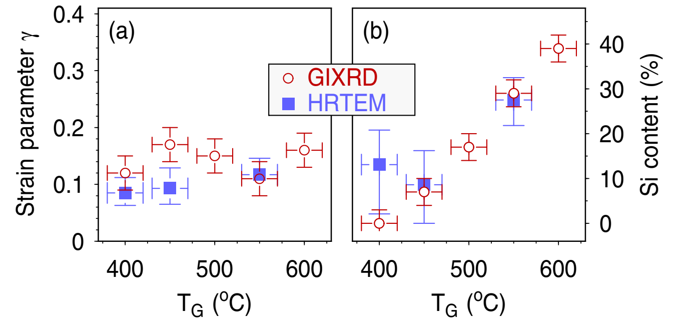

FIG. 16. Growth temperature dependence (a) of the strain parameter and (b) of the average Si content of the Ge islands, as determined from GIXRD (○) and high-resolution TEM (■).

and thus in dependence of the strain parameter

$$\gamma = \frac{a_\parallel - a_\parallel^{\mathrm{bulk}}(x)}{a_{\parallel,\mathrm{Si}}^{\mathrm{bulk}} - a_\parallel^{\mathrm{bulk}}(x)}\,, \quad (4)$$

where $\gamma = 0$ corresponds to completely relaxed $\mathrm{Ge}_x\mathrm{Si}_{1-x}$ and $\gamma = 1$ to pseudomorphically strained $\mathrm{Ge}_x\mathrm{Si}_{1-x}$. By comparison of the calculated $a_\perp$ and $a_\parallel$ values to the experimentally determined ones, γ and x can numerically be identified. The results are illustrated by open dots in Fig. 16. (For comparison, respective results from high-resolution TEM, which will be discussed below, are represented by solid squares.) Virtually no Si is incorporated into the islands at a growth temperature of 400 °C, whereas the average Si concentration is increased to $c_{\mathrm{Si}} = 39\%$ at 600 °C. For the strain parameter, values between 0.11 and 0.17 are obtained from GIXRD; however, there is no clear tendency in dependence on T_G. Within the error bar, γ could be considered constant within the investigated temperature range and the change of the Ge Bragg spot positions described above to be almost solely caused by Ge/Si intermixing. Nevertheless, the GIXRD strain state analysis reveals that on average more than 80% of the strain induced by lattice mismatch is relieved in the islands.

Returning to the RSMs shown in Fig. 15, it is noteworthy that no thickness fringes are observed along the Ge(20) CTR. Such thickness oscillations are expected for a smooth Ge film of uniform thickness and have been reported for Sb and Bi mediated Ge growth on Si(111) at comparable Ge deposit [23,27]. Since from the LEED and LEEM results discussed in Secs. III B and III C it can be assumed that the islands exhibit smooth (111) top facets; the lack of thickness fringes can be attributed to a relatively broad distribution of island heights.

An additional Bragg spot appears on the Ge(20) CTR of all samples at $l \approx 1.3$, to be seen at the bottom part of the RSMs in Fig. 15. For the diamond crystal structure, no such Bragg structure is expected. The vertical position of this spot corresponds to that of the Ge(004) Bragg reflection located on the Ge($\bar{2}$0) CTR (see shaded areas in Fig. 14). Therefore, it is concluded that the CTR intensity observed in the experiment is a superposition of the Ge(20) CTR signal from regularly stacked ("A-type") island material and of the Ge($\bar{2}$0) CTR intensity from twinned ("B-type") domains in the islands, i.e.,

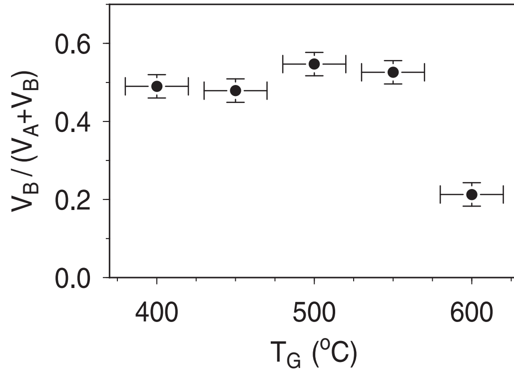

FIG. 17. Growth temperature dependence of the volume fraction of twinned Ge.

from regions where the crystal structure is rotated by 180° around the (111) direction with respect to the substrate lattice.

Within the kinematic approximation, the integral diffracted intensity $I_{A,B}$ from the A-type and B-type domains is proportional to the total volumes $V_{A,B}$ of the respective domains and the structure factor $|F_{A,B}|^2$ of the respective Bragg reflection. Hence, an estimate of the volume fraction of B-type material is given by

$$\frac{V_B}{V_A + V_B} = \left(1 + \left|\frac{F_A}{F_B}\right|^2 \frac{I_A}{I_B}\right)^{-1}. \tag{5}$$

The integral intensities I_A and I_B have been determined from scans along the Ge(20) CTR, such as shown in Fig. 15, and additional scans in the $Q_\parallel$ planes (not shown here) at the $Q_\perp$ positions of the corresponding Bragg spots. Regarding the structure factor ratio F_A/F_B, it was assumed that the chemical composition of A-type and B-type domains are the same, which is justified by the fact that the lateral and also the vertical lattice parameters of both domains coincide with each other within the experimental resolution (see Fig. 15). For equal chemical composition, the structure amplitude ratio F_A/F_B for a random Ge_xSi_{1-x} alloy is virtually independent of the atomic scattering amplitudes of Ge and Si, and thus, of x. In the present case, we used $|F_{(33\bar{1})}/F_{(004)}|^2 = 0.45$. The results for the twinned volume fraction determined according to Eq. (5) are presented in Fig. 17. It is obvious that at relatively low growth temperatures about half of the material in the islands is of B type, which implies a dramatically reduced crystal quality. Notably, the same finding, namely a 1:1 ratio of A to B type material, has been reported for Ga mediated Ge/Si(111) epitaxy [21]. From $T_G = 550\,^\circ$C to $T_G = 600\,^\circ$C, however, the fraction of B-type material is significantly decreased. This is understood in terms of thermal activation, which at higher T_G prevents the formation of stacking faults that occurs, conversely, due to kinetic limitations at lower T_G. For $T_G \leqslant 550\,^\circ$C, the data in Fig. 17 do not show a strong temperature dependence and, within the experimental uncertainty, the fraction of twinned material might be considered as constant in this temperature range. On the other hand, also a slight increase of the twinned material at medium temperatures might be identified from Fig. 17. The latter could be explained by the onset of Ge/Si intermixing that has been evidenced above. In a growth regime where the Ge crystal quality is kinetically limited, increasing incorporation of (less mobile) Si can be expected to lead to further enhanced defect formation. Moreover, stacking fault formation can be expected to be enhanced for increasing Si content from an energetic point of view, since the stacking fault energy of Si is only around half of that of Ge [94]. Both the kinetic and energetic favoring of stacking fault formation with increasing Si content (relative to pure Ge) could also explain the still relatively high B-type fraction of about 20% at 600 °C. For comparison, hardly any twins (below about 1% volume fraction) were observed at $T_G = 600\,^\circ$C in the case of Sb mediated SME [27], where Ge/Si intermixing is negligible [36,95].

The defect structure observed by GIXRD is resolved on atomic scale by TEM. In Fig. 18(a), a high-resolution TEM image (HRTEM) in $[1\bar{1}0]$ zone axis for a sample prepared at 550 °C is shown, taken at the edge of a Ge island. Clearly, the interface between Ge and Si as well as the side facet of the island can be seen. The orientation of such facets could not be determined in the LEED experiments described above, since they occupy a very small fraction of the surface only. From the HRTEM data, an inclination angle slightly above 40° with respect to the (111) surface is observed. Assuming a facet normal to the projection plane of the image, this value is indicative of a $(55\bar{1})$ facet. The nearest low-index orientation, with 35.3° inclination, is a (110) orientation.

Figures 18(b) and 18(c) depict diffractograms that have been computed by Fourier transform from different regions of the HRTEM image shown in Fig. 18(a). The diffractogram from the substrate region [Fig. 18(b)] shows peaks at the Bragg spot positions expected for the diamond lattice [cf. Fig. 14; note that the diffractograms in Figs. 18(b) and 18(c) are not true diffraction patterns but are computed from real-space images]. The corresponding diffractogram from the Ge island region in Fig. 18(c) exhibits additional spots, which can be generated by a mirror operation. Therefore, these spots can be assigned to B-oriented domains within the Ge islands, which are, with respect to the the A-type orientation of the substrate, rotated by 180° around the (111) axis, as has already been argued for the GIXRD data above.

The TEM data in Fig. 18 provides an insight into the real-space distribution of A-type and B-type domains within the Ge film. This is illustrated in Fig. 18(d), where the part marked by a dashed square in the HRTEM image of Fig. 18(a) is presented after Fourier filtering, which has been accomplished by selecting respective diffractogram reflections using circular masks and applying a Wiener noise filter [96,97]. All but the (000), the $(11\bar{1})_A$, and the $(11\bar{1})_B$ Fourier components have been suppressed in Fig. 18(d), hence, the $(11\bar{1})$ lattice fringes of both the A-type and the B-type regions become clearly visible in this artificial lattice fringe image, making the A and B domains more easily distinguishable. From these data, no clear preference for A-type or B-type Ge material is found. A-type Ge grows on top of B-type Ge, and vice versa. At some places, both $(11\bar{1})_A$, and $(11\bar{1})_B$ lattice fringes are superimposed. This is explained by A-type and B-type regions coexisting along the $[1\bar{1}0]$ zone axis.

In addition to stacking faults at the interface between A-type and B-type domains, interfacial misfit dislocations are also

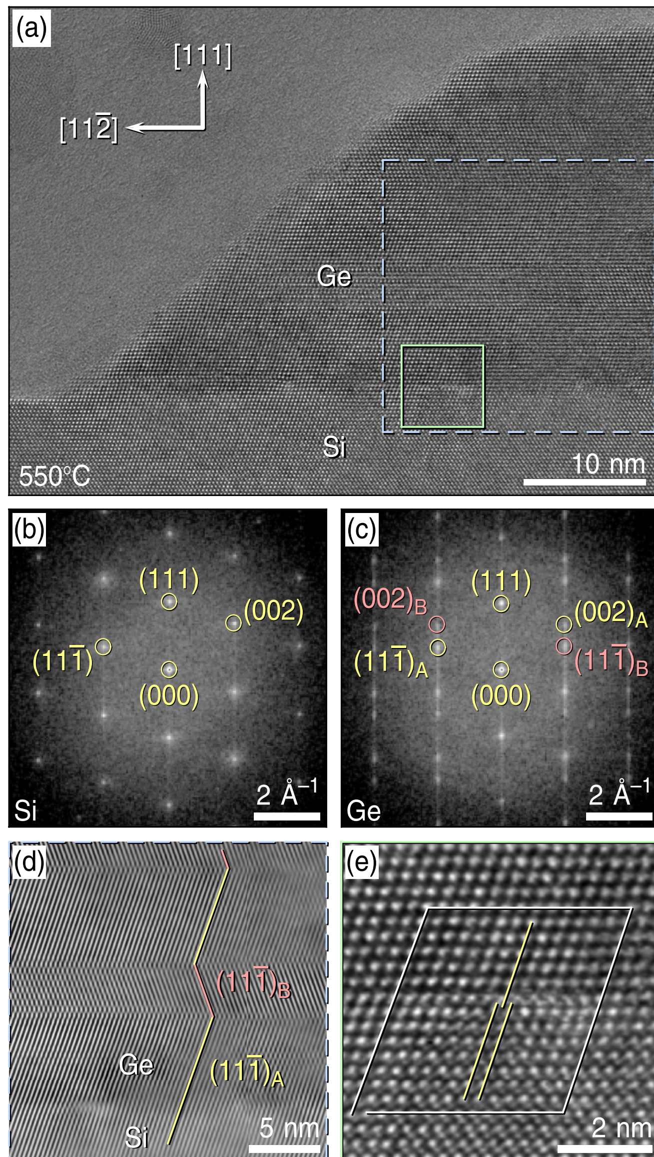

FIG. 18. (a) High-resolution transmission electron microscopy (HRTEM) image of a Ge island on a sample prepared at 550 °C, recorded in [1$\bar{1}$0] zone axis. (b) Diffractogram (Fourier transform) of the substrate region of the HRTEM image in (a). (c) Diffractogram of the island region in (a). (d) Fourier filtered image of the region marked with dashed square in (a), emphasizing A-type and B-type orientation. (e) Zoom into region marked with solid square in (a), exposing a dislocation.

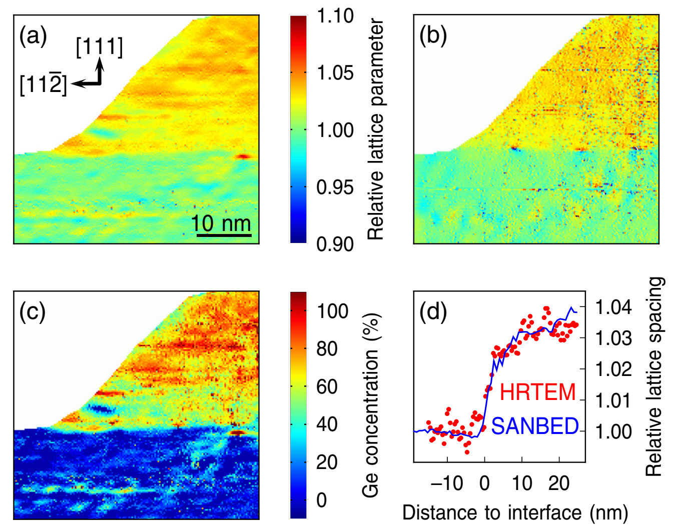

FIG. 19. Local (a) vertical and (b) lateral lattice parameters in units of the bulk Si lattice parameters, as determined from HRTEM, and (c) corresponding composition map, for the sample area shown in Fig. 18(a), i.e., for a growth temperature of 550 °C; (d) comparison of local vertical lattice parameter [normalized to the bulk Si(111) layer spacing] as determined by HRTEM (dots) and by SANBED (solid line).

revealed by HRTEM. Figure 18(e) shows a zoom into the region marked with a solid square in Fig. 18(a). While on the left-hand side as well as on the right-hand side of Fig. 18(e) the (11$\bar{1}$) lattice planes are continuous across the Ge/Si interface, they appear interleaved at the misfit dislocation in the middle of the image, as indicated by the straight lines. Two Si lattice planes are facing one Ge lattice plane.

A Burgers circuit (solid line) is drawn around the MD. The missing piece at the bottom left represents the projection of the Burgers vector into the image plane. It is determined to $\vec{b}_{\parallel} = [11\bar{2}]a_0/4$. The Burgers vector component $\vec{b}_{\perp} || [1\bar{1}0]$ along the electron beam, i.e., perpendicular to the image plane, cannot be quantified from the data. For fcc and diamond lattices in general, and in particular for Ge on Si [98–101], possible dislocations discussed in literature are (i) the perfect dislocations $\vec{b} = \langle 1\bar{1}0\rangle a_0/2$ and (ii) the Shockley partial dislocations $\vec{b} = \langle 11\bar{2}\rangle a_0/6$. The latter can be ruled out from the observed value of $\vec{b}_{\parallel}$, whereas our data complies with the former ones, if $\vec{b}_{\perp} = \pm[1\bar{1}0]a_0/4$ is assumed. The resulting Burgers vectors $\vec{b} = [10\bar{1}]a_0/2$ and $\vec{b} = [01\bar{1}]a_0/2$ correspond to a perfect 60° dislocation [101]. Judging from Fig. 18(e), it might also be possible that this perfect dislocation has dissociated into two Shockley partial dislocations that are both contained in the Burgers circuit, with a small stacking fault region in between.

In order to assess the local chemistry, we applied strain state analysis to the HRTEM images in both the growth and lateral direction and compared the results with elasticity theory. In particular, (111) and (11$\bar{1}$) lattice fringe images have been obtained by Fourier filtering of HRTEM images such as shown in Fig. 18(a), selecting respective diffractogram reflections and transforming back to real space. Again, a Wiener noise filter has been applied. Intensity maxima have been identified horizontally in the (11$\bar{1}$) and vertically in the (111) fringe images, with subpixel accuracy achieved by parabolian fitting. Local distances between adjacent maxima along [111] have been determined and normalized to their average in pure Si, as shown exemplarily for $T_G = 550$ °C in Fig. 19(a). Similarly, lateral distances were determined from the vectors connecting neighbored maxima in the (11$\bar{1}$) fringe images. As [11$\bar{1}$] is not perpendicular to [111], the projections of the connection vectors onto [11$\bar{2}$] were used instead. Again, the result was normalized to the corresponding value in pure Si and is shown in Fig. 19(b).

Since HRTEM images are subject to imaging artifacts arising from aberrations of the objective lens as well as gradients

of the specimen thickness and the chemical composition, we cross-checked the HRTEM results with strain analysis by nanobeam electron diffraction (SANBED), which solely relies on Bragg's law [102,103]. Figure 19(d) shows the local (111) layer spacing obtained by evaluating the distance between the undiffracted beam and the (111) reflection using the selective edge detection algorithm [102] while scanning over the Ge island in Fig. 18(a), in comparison to a HRTEM vertical lattice parameter profile from Fig. 19(a). Within the precisions of both methods (9×10^{-4} for SANBED and 5×10^{-3} for HRTEM in the present study), the results are in excellent agreement. In this respect, the SANBED data might be preferable for strain state analysis. However, the twinned domains lead to overlapping $(11\bar{1})_A$ and $(002)_B$ diffraction discs near domain boundaries which precludes the data from obtaining reliable strain measurements in the lateral direction. Note that the diameter of the STEM probe for SANBED was approximately 1 nm, such that the spatial resolution is an order of magnitude worse than in HRTEM in the present study.

By combining data such as shown in Figs. 19(a) and 19(b) with reference values obtained from elasticity theory (as described above), Ge composition maps have been compiled as shown exemplarily for $T_G = 550\,^\circ$C in Fig. 19(c). Obviously, the Ge content increases gradually in growth direction up to values of approximately 0.7 to 0.8. Because of the limited thickness of the TEM specimen in electron beam direction, the stress along the $[1\bar{1}0]$ zone axis, $\sigma_{1\bar{1}0}$, might differ from the stress in the transverse lateral direction, $\sigma_{11\bar{2}}$. In regard of the high symmetry of the (111) interface plane, the parameter $r_\perp$ in the relation $\sigma_{1\bar{1}0} = r_\perp \sigma_{11\bar{2}}$ can take values from zero (complete relaxation along zone axis) to unity (isotropic lateral stress). Here and in the following, results for a relative transverse lateral stress of $r_\perp = 0.5$ are presented. According analyses for the extreme cases, $r_\perp = 0$ and $r_\perp = 1$, have also been performed in order to assess the systematic uncertainty related to the unknown strain state along the electron beam direction, as detailed below.

To study the influence of the growth temperature on the Ge incorporation in more detail, concentration profiles in the [111] direction have been extracted from HRTEM data for samples grown at 400 °C, 450 °C, and 550 °C. The results are depicted in Fig. 20. In all cases, there is a gradual increase of the Ge concentration, which then reaches a saturation value near the top of the islands. For growth temperatures of 400 °C and 450 °C, the Ge concentration saturates at values close to unity, whereas for 550 °C a significantly lower saturation value is obvious from the data. For a quantitative comparison, the profiles have been fitted according to the segregation model proposed by Muraki *et al.* [104] The resulting fits are superimposed as solid lines in Fig. 20. The data are well described by this phenomenological model, which, in our case, predicts a Ge concentration $x(n)$ in the nth layer of

$$x(n) = \begin{cases} 0 & \text{for} \quad n < 1 \\ x_0(1 - R^n) & \text{for} \quad n \geqslant 1 \end{cases}, \tag{6}$$

where R denotes a segregation efficiency and x_0 the saturation concentration. Our analysis supports almost pure Ge at the top of the islands ($x_0 \approx 0.9$) for growth temperatures of 400 °C and 450 °C, whereas a significantly lower value of $x_0 = 0.73$ is indicated for $T_G = 550\,^\circ$C. Moreover, the segregation

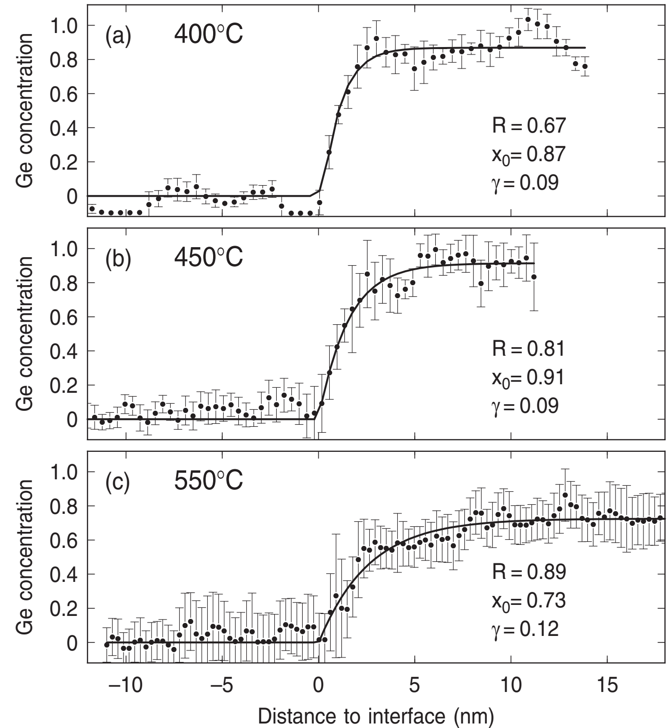

FIG. 20. Ge concentration profiles along growth direction for growth temperatures of (a) 400 °C, (b) 450 °C, and (c) 550 °C. Dots represent the local Ge concentration as determined from HRTEM data, the solid lines are a numerical fit to the Muraki model [104] [cf. Eq. (6)]. The values of R, x_0, and of the strain parameter γ [cf. Eq. (4)] are indicated in each frame.

efficiency R shows a monotonic decrease towards lower T_G, which results in sharper interfaces and, thus, in steeper edges of the profiles in Fig. 20. This is indicative of thermally activated segregation or intermixing.

In order to compare the Ge content determined by HRTEM with the results from GIXRD, the values corresponding to x_0 from the Muraki fits are superimposed in Fig. 16(b). We note that the *average* Ge content is slightly lower than x_0, since according to Fig. 20 there are volumes with significantly lower Ge content near the interface. Nevertheless, these regions are very thin and have a relatively large gradient of the lattice parameter, and hence, give only rise to a weak and broadened signal in GIXRD, while the intense Ge Bragg peaks evaluated in the GIXRD analysis originate from the thicker regions with more uniform lattice parameter and more homogeneous Ge content very close to x_0. The relatively large error bars for the HRTEM results in Fig. 16(b) are due to the uncertainty of the relative transverse lateral stress $r_\perp$, as explained above. Within this uncertainty, the results from GIXRD and HRTEM as shown in Fig. 16(b) are in very good agreement.

Not only the Ge concentration, but also the strain parameter γ [cf. Eq. (4)] can be quantified from the relative lateral and vertical lattice constants. In contrast to the Ge content, however, neither does the *local* strain parameter (not depicted here) show a clear dependence on the distance from the interface, nor does the *average* strain parameter (indicated in Fig. 20) show a clear trend with growth temperature. Instead, values around $\gamma = 0.1$ are obtained in all cases, indicative of

almost complete relaxation. The values of the average strain parameter according to the HRTEM analysis are compared to respective results from GIXRD in Fig. 16(a). Again, a good agreement is found.

F. Suitability of Ag as a surfactant

In the previous sections it has been shown that Ge growth on Ag/Si(111)-$\sqrt{3}\times\sqrt{3}$-R 30° differs significantly from the epitaxy of Ge on Si(111)-7×7. Already the Ge wetting layer growth is different from that found for growth on bare Si substrates. Instead of a layer-by-layer growth mode with homogeneous nucleation of two-dimensional Ge islands [10,105], a heterogeneous wetting layer nucleation is observed on Ag/Si(111)-$\sqrt{3}\times\sqrt{3}$-R 30°, where the internal step edges of the maze structure serve as nucleation centers. Even after the trenches of the maze structure have been filled with Ge, the next Ge layer does not form compact two-dimensional islands but exhibits a modified step-flow growth. At the growth temperatures used here, and for terrace widths in the micron range, the fact that a step-flow-like growth mode is observed points to a largely increased diffusion length for Ge on the Ag-$\sqrt{3}\times\sqrt{3}$-R 30° terminated surface. Instead of a classical step-flow growth, a rather dendritic flavor of step flow is found, which is attributed to the patterned surface strain and chemistry of the filled-up maze structure that comprises Ag/Ge/Si and Ag/Si patches.

Like for Ge growth on clean Si substrates, three-dimensional islands are formed on the wetting layer in case of growth on Ag/Si(111)-$\sqrt{3}\times\sqrt{3}$-R 30°. However, these islands do not show a pyramidal or dome shape with mainly (113) facets as reported for Ge growth on bare Si(111) and Si(001) [5,8,71,106], but they are rather flat with a huge top (111) facet. These islands grow on the expense of the wetting layer, which seems to be a general scheme that has also been observed, e.g., for Bi-mediated Ge growth on Si(111) [107].

In some respects, Ag behaves like a typical surfactant. Using XPEEM, Ag has been demonstrated to efficiently segregate to the surface, the driving force for which is probably a reduction of the surface free energy by Ag termination. The degree of lattice relaxation found with LEED and GIXRD is similar to that observed for Sb or Bi mediated epitaxy [27,28]. Also the defect structure is similar, with interfacial misfit dislocations as well as twinning, the latter being largely suppressed at higher growth temperatures. For Ag, however, the increase in structural quality is accompanied by Ge/Si alloying, as revealed by GIXRD and TEM.

Silver has a strong impact on the growth kinetics. This does not only influence the wetting layer growth as mentioned above, but also leads to a drastic *increase* of the diffusion length at later growth stages. In our reference experiments without Ag preadsorption, we find island densities that are larger by about three orders of magnitude under the same growth conditions. This is in clear contrast to the commonly used group-V surfactants As, Sb, and Bi that tend to *reduce* the effective diffusion length [17,18].

The large diffusion length of Ge on a Ag-$\sqrt{3}\times\sqrt{3}$-R 30° terminated Ge wetting layer is the main reason that makes Ag inferior to the conventional surfactants in terms of surface morphology. Though the huge flat Ge islands have been shown to coalesce at a Ge deposit Θ_{Ge} of roughly 20 BL, no continuous Ge film (except for the wetting layer) can be expected for a thickness below $\Theta_{Ge} \approx 66$ BL at the growth conditions used in this work. For comparison, a smooth, continuous Ge film is obtained at $\Theta_{Ge} \approx 9$ BL in the case of Sb-mediated epitaxy [93]. Hence, for ultrathin Ge layers, Ag is not the surfactant of choice. For applications, however, that require slightly thicker films, Ag might indeed offer a promising alternative.

Silver might also be useful when combining surfactant mediated epitaxy with artificial substrate patterning techniques such as lithography, e.g., for the growth of thin Ge films on mesa structures. Such micron-scale structures match the typical Ge island diameter in the case of Ag SME very well, and thus, delayed island coalescence, as experienced here on macroscopic surfaces, becomes meaningless.

Silver might even be superior to conventional group-V surfactants if suppression of unintentional doping is the main concern, since Ag has a lower solubility in Ge and forms deep localization centers with an ionization energy of 130 meV. In comparison, Sb and Bi are shallow impurities [38] with ionization energies below 15 meV.

IV. CONCLUSION

The preadsorption of Ag has significant impact on subsequent Ge growth, as our approach combining microscopy, diffraction, and spectroscopy techniques has shown. Both the wetting layer growth as well as the subsequent island growth are very different from Ge growth on bare Si(111). A key feature of the Ag mediated Ge growth is a strongly increased Ge surface diffusion length that is reflected by a very low density of very wide and flat islands. This morphology is not typical of Ge/Si three-dimensional island growth and could better be described as a noncontinuous film growth mode. The coalescence of the flat islands, which will finally lead to a continuous film, takes place at a rather late growth stage (with a "critical" film thickness of about 20 to 30 nm), as compared to other surfactants. The lattice mismatch is accommodated to a large extent by a hexagonal network of misfit dislocations. In addition, stacking faults have been identified as a common defect type, which leads to the formation of twinned Ge regions. The abundance of stacking faults can drastically be reduced at higher growth temperatures T_G around 600 °C. This has also been reported for Sb mediated Ge/Si(111) epitaxy [27]. However, in the present case of Ag as a surfactant, Ge/Si intermixing becomes more pronounced with increasing T_G, with up to 40% Si content in the film for $T_G = 600$ °C. Nevertheless, our results suggest that Ag might be a superior alternative to conventional surfactants for specific applications, e.g., the growth of thin Ge films with low doping level on mesa structures for small devices.

ACKNOWLEDGMENTS

This work has been supported by the Deutsche Forschungsgemeinschaft (Grants No. FA 363/6 and No. MU 3660/1–1) and by the physics international postgraduate (PIP) programme of the University of Bremen (supported by the German Academic Exchange Service).

[1] D. Reinking, M. Kammler, N. Hoffmann, M. Horn-von Hoegen, and K. R. Hofmann, Electron. Lett. **35**, 503 (1999).
[2] A. Dobbie, V. H. Nguyen, M. Myronov, T. E. Whall, E. H. C. Parker, and D. R. Leadley, Appl. Phys. Expr. **5**, 071301 (2012).
[3] E. Gatti, F. Isa, D. Chrastina, E. Müller Gubler, F. Pezzoli, E. Grilli, and G. Isella, J. Appl. Phys. **116**, 043518 (2014).
[4] H. Ye and J. Yu, Sci. Technol. Adv. Mater. **15**, 024601 (2014).
[5] P. M. J. Maree, K. Nakagawa, F. M. Mulders, J. F. van der Veen, and K. L. Kavanagh, Surf. Sci. **191**, 305 (1987).
[6] Y. W. Mo, B. S. Swartzentruber, R. Kariotis, M. B. Webb, and M. G. Lagally, Phys. Rev. Lett. **63**, 2393 (1989).
[7] D. J. Eaglesham and M. Cerullo, Phys. Rev. Lett. **64**, 1943 (1990).
[8] F. M. Ross, R. M. Tromp, and M. C. Reuter, Science **286**, 1931 (1999).
[9] P. Sheldon, B. G. Yacobi, K. M. Jones, and D. J. Dunlavy, J. Appl. Phys. **58**, 4186 (1985).
[10] U. Köhler, O. Jusko, G. Pietsch, B. Müller, and M. Henzler, Surf. Sci. **248**, 321 (1991).
[11] M. Copel, M. C. Reuter, E. Kaxiras, and R. M. Tromp, Phys. Rev. Lett. **63**, 632 (1989).
[12] F. K. LeGoues, M. Copel, and R. M. Tromp, Phys. Rev. B **42**, 11690 (1990).
[13] E. Kaxiras, Europhys. Lett. **21**, 685 (1993).
[14] J. Massies and N. Grandjean, Phys. Rev. B **48**, 8502 (1993).
[15] R. M. Tromp and M. C. Reuter, Phys. Rev. Lett. **68**, 954 (1992).
[16] B. Voigtländer and A. Zinner, J. Vac. Sci. Technol. A **12**, 1932 (1994).
[17] B. Voigtländer, A. Zinner, T. Weber, and H. P. Bonzel, Phys. Rev. B **51**, 7583 (1995).
[18] K. Schroeder, B. Engels, P. Richard, and S. Blügel, Phys. Rev. Lett. **80**, 2873 (1998).
[19] K. Schroeder, A. Antons, R. Berger, and S. Blügel, Phys. Rev. Lett. **88**, 046101 (2002).
[20] R. Zhachuk and J. Coutinho, Surf. Sci. **647**, 12 (2016).
[21] J. Falta, M. Copel, F. K. LeGoues, and R. M. Tromp, Appl. Phys. Lett. **62**, 2962 (1993).
[22] G. Meyer, B. Voigtländer, and N. M. Amer, Surf. Sci. **274**, L541 (1992).
[23] Th. Schmidt, J. Falta, G. Materlik, J. Zeysing, G. Falkenberg, and R. L. Johnson, Appl. Phys. Lett. **74**, 1391 (1999).
[24] M. Horn-von Hoegen, F. K. LeGoues, M. Copel, M. C. Reuter, and R. M. Tromp, Phys. Rev. Lett. **67**, 1130 (1991).
[25] M. Horn-von Hoegen, A. Al-Falou, H. Pietsch, B. H. Müller, and M. Henzler, Surf. Sci. **298**, 29 (1993).
[26] A. Janzen, I. Dumkow, and M. Horn-von Hoegen, Appl. Phys. Lett. **79**, 2387 (2001).
[27] Th. Schmidt, R. Kröger, T. Clausen, J. Falta, A. Janzen, M. Kammler, P. Kury, P. Zahl, and M. Horn-von Hoegen, Appl. Phys. Lett. **86**, 111910 (2005).
[28] Th. Schmidt, R. Kröger, J. I. Flege, T. Clausen, J. Falta, A. Janzen, P. Zahl, P. Kury, M. Kammler, and M. Horn-von Hoegen, Phys. Rev. Lett. **96**, 066101 (2006).
[29] T. Clausen, J.-I. Flege, Th. Schmidt, and J. Falta, Proc. Mat. Res. Soc. Symp. **910**, Ra12.06 (2005).
[30] T. F. Wietler, E. Bugiel, and K. R. Hofmann, Thin Solid Films **517**, 272 (2008).
[31] K. N. Romanyuk, A. A. Shklyaev, and B. Z. Olshanetsky, Surf. Sci. **617**, 68 (2013).
[32] T. F. Wietler, J. Schmidt, D. Tetzlaff, and E. Bugiel, Thin Solid Films **557**, 27 (2014).
[33] D. Reinking, M. Kammler, M. Horn-von Hoegen, and K. R. Hofmann, J. Appl. Phys. **36**, L1082 (1997).
[34] J. Falta, T. Gog, G. Materlik, B. H. Müller, and M. Horn-von Hoegen, Phys. Rev. B **51**, 7598 (1995).
[35] J. Falta, D. Bahr, G. Materlik, B. H. Müller, and M. Horn-von Hoegen, Appl. Phys. Lett. **68**, 1394 (1996).
[36] P. Zahl, P. Kury, and M. Horn-von Hoegen, Appl. Phys. A **69**, 481 (1999).
[37] D. Reinking, M. Kammler, M. Horn-von Hoegen, and K. R. Hofmann, Appl. Phys. Lett. **71**, 924 (1997).
[38] O. Madelung, *Semiconductors — basic data*, 2nd ed. (Springer Verlag, Berlin, 1996).
[39] S. P. Murarka, Annu. Rev. Mater. Sci. **13**, 117 (1983).
[40] M. E. Schlesinger, Chem. Rev. **90**, 607 (1990).
[41] A. B. Gokhale and G. J. Abbaschian, Bull. Alloy Phase Diagrams **7**, 333 (1986).
[42] N. N. Greenwood and A. Earnshaw, *Chemistry of the Elements*, 2nd ed. (Elsevier Science, Oxford, 1997).
[43] H. L. Gaigher and N. van der Berg, Thin Solid Films **68**, 373 (1980).
[44] L. Topor and O. Kleppa, J. Less-Common Met. **167**, 91 (1990).
[45] F. P. Netzer, J. Phys.: Condens. Matter **7**, 991 (1995).
[46] P. A. Bennett, Z. He, D. J. Smith, and F. M. Ross, Thin Solid Films **519**, 8434 (2011).
[47] J. A. Kanpp and S. T. Picraux, Appl. Phys. Lett. **48**, 466 (1986).
[48] I. Mayer and I. Felner, J. Phys. Chem. Solids **38**, 1031 (1977).
[49] T. Watahiki, B. P. Tinkham, B. Jenichen, R. Shayduk, W. Braun, and K. H. Ploog, Appl. Surf. Sci. **255**, 758 (2008).
[50] P. J. Godowski, F. Ørskov, M. Christiansen, and J. Onsgaard, Thin Solid Films **205**, 35 (1991).
[51] H. Okamoto, J. Phas. Equil. Diff. **28**, 585 (2007).
[52] A. Munitz, A. B. Gokhale, and G. J. Abbschain, Bull. Alloy Phase Diagrams **10**, 73 (1989).
[53] A. B. Gokhale, A. Munitz, and G. J. Abbschain, Bull. Alloy Phase Diagrams **10**, 246 (1989).
[54] R. W. Olesinski and G. J. Abbaschian, Bull. Alloy Phase Diagrams **6**, 545 (1985).
[55] R. W. Olesinski and G. J. Abbaschian, Bull. Alloy Phase Diagrams **6**, 534 (1985).
[56] C. Guminski, J. Phase Equilib. **22**, 682 (2001).
[57] R. W. Olesinski and G. J. Abbaschian, Bull. Alloy Phase Diagrams **10**, 635 (1989).
[58] R. W. Olesinski and G. J. Abbaschian, Bull. Alloy Phase Diagrams **9**, 58 (1988).
[59] G. LeLay, Surf. Sci. **132**, 169 (1983).
[60] R. J. Wilson and S. Chiang, Phys. Rev. Lett. **58**, 369 (1987).
[61] S. Tosch and H. Neddermeyer, Phys. Rev. Lett. **61**, 349 (1988).
[62] Y. G. Ding, C. T. Chan, and K. M. Ho, Phys. Rev. Lett. **67**, 1454 (1991).
[63] K. J. Wan, X. F. Lin, and J. Nogami, Phys. Rev. B **47**, 13700 (1993).
[64] M. Horn-von Hoegen, Th. Schmidt, M. Henzler, G. Meyer, D. Winau, and K. H. Rieder, Surf. Sci. **331-333**, 575 (1995).
[65] S. Fölsch, G. Meyer, D. Winau, K. H. Rieder, M. Horn-von Hoegen, Th. Schmidt, and M. Henzler, Phys. Rev. B **52**, 13745 (1995).
[66] K. Sakamoto, H. Ashima, H. M. Zhang, and R. I. G. Uhrberg, Phys. Rev. B **65**, 045305 (2001).

[67] I. Matsuda, H. Morikawa, C. Liu, S. Ohuchi, S. Hasegawa, T. Okuda, T. Kinoshita, C. Ottaviani, A. Cricenti, M. D'angelo, P. Soukiassian, and G. Le Lay, Phys. Rev. B **68**, 085407 (2003).

[68] F. Ming, K. Wang, S. Pan, J. Liu, Y. Zhang, J. Yang, and X. Xiao, ACS Nano **5**, 7608 (2011).

[69] A. E. Dolbak and B. Z. Ol'shanetskii, J. Exp. Theor. Phys. **116**, 952 (2013).

[70] T. Yamagami, J. Sone, K. Nakatsuji, and H. Hirayama, Appl. Phys. Lett. **105**, 151603 (2014).

[71] Th. Schmidt, M. Speckmann, J. Falta, T. O. Menteş, M. Á. Niño, and A. Locatelli, e-J. Surf. Sci. Nanotech. **8**, 221 (2010).

[72] J. C. Mahato, D. Das, B. Bisi, A. Pal, and B. N. Dev, Appl. Surf. Sci. **356**, 249 (2015).

[73] J. Falta, Th. Schmidt, A. Hille, and G. Materlik, Phys. Rev. B **54**, R17288 (1996).

[74] A. Locatelli, A. Bianco, D. Cocco, S. Cherifi, S. Heun, M. Marsi, M. Pasqualetto, and E. Bauer, J. Phys. IV (France) **104**, 99 (2003).

[75] A. Locatelli, L. Aballe, T. O. Menteş, M. Kiskinova, and E. Bauer, Surf. Interface Anal. **38**, 1554 (2006).

[76] T. O. Menteş, G. Zamborlini, A. Sala, and A. Locatelli, Beilstein J. Nanotechnol. **5**, 1873 (2014).

[77] K. D. Gronwald and M. Henzler, Surf. Sci. **117**, 180 (1981).

[78] M. Horn-von Hoegen, Z. Kristallogr. **214**, 1 (1999).

[79] M. Speckmann, Th. Schmidt, J. I. Flege, J. T. Sadowski, P. Sutter, and J. Falta, J. Phys.: Condens. Matter **21**, 314020 (2009).

[80] M. Horn-von Hoegen, Appl. Phys. A **59**, 503 (1994).

[81] M. Lohmeier and E. Vlieg, J. Appl. Crystallogr. **26**, 706 (1993).

[82] A. Bergamaschi, A. Cervellino, R. Dinapoli, F. Gozzo, B. Henrich, I. Johnson, P. Kraft, A. Mozzanica, B. Schmitt, and X. Shi, J. Synchrotron Radiat. **17**, 653 (2010).

[83] Th. Schmidt, S. Gangopadhyay, J. I. Flege, T. Clausen, A. Locatelli, S. Heun, and J. Falta, New J. Phys. **7**, 193 (2005).

[84] Th. Schmidt, J. I. Flege, S. Gangopadhyay, T. Clausen, A. Locatelli, S. Heun, and J. Falta, Phys. Rev. Lett. **98**, 066104 (2007).

[85] E. Bauer, Rep. Prog. Phys. **57**, 895 (1994).

[86] K. Takayanagi, Y. Tanishiro, M. Takahashi, and S. Takahashi, J. Vac. Sci. Technol. A **3**, 1502 (1985).

[87] R. M. Tromp and M. C. Reuter, Phys. Rev. B **47**, 7598 (1993).

[88] D. Grozea, E. Bengu, and L. D. Marks, Surf. Sci. **461**, 23 (2000).

[89] S. Tanuma, C. J. Powell, and D. R. Penn, Surf. Interface Anal. **17**, 911 (1991).

[90] B. Henke, E. Gullikson, and J. Davis, At. Data Nucl. Data Tables **54**, 181 (1993).

[91] F. Ratto, F. Rosei, A. Locatelli, S. Cherifi, S. Fontana, S. Heun, P. D. Szkutnik, A. Sgarlata, M. de Crescenzi, and N. Motta, Appl. Phys. Lett. **84**, 4526 (2004).

[92] F. Ratto, F. Rosei, A. Locatelli, S. Cherifi, S. Fontana, S. Heun, P. D. Szkutnik, A. Sgarlata, M. de Crescenzi, and N. Motta, J. Appl. Phys. **97**, 043516 (2005).

[93] M. Horn-von Hoegen, M. Pook, A. Al-Falou, B. H. Müller, and M. Henzler, Surf. Sci. **284**, 53 (1993).

[94] P. J. H. Denteneer and W. van Haeringen, J. Phys. C **20**, L883 (1987).

[95] M. Horn-von Hoegen, M. Copel, J. C. Tsang, M. C. Reuter, and R. M. Tromp, Phys. Rev. B **50**, 10811 (1994).

[96] W. H. Press, W. T. Vetterling, S. A. Teukolsky, and B. P. Flannery, *Numerical Recipes in C*, 1st ed. (Cambridge University Press, Cambridge, 1992), p. 58.

[97] A. Rosenauer, *Transmission Electron Microscopy of Semiconductor Nanostructures — An Analysis of Composition and Strain State*, Springer tracts in modern Physics, Vol. 182 (Springer, Berlin, Heidelberg, 2003).

[98] F. Ernst, P. Pirouz, and E. Bauser, Phys. Status Solidi A **131**, 651 (1992).

[99] O. Hansson, F. Ernst, and E. Bauser, J. Appl. Phys. **72**, 2083 (1992).

[100] M. Dornheim and H. Teichler, Phys. Status Solidi B **222**, 101 (2000).

[101] A. T. Blumenau, R. Jones, and T. Frauenheim, J. Phys.: Condens. Matter **15**, S2951 (2003).

[102] K. Müller, A. Rosenauer, M. Schowalter, J. Zweck, R. Fritz, and K. Volz, Microsc. Microanal. **18**, 995 (2012).

[103] K. Müller-Caspary, A. Oelsner, and P. T. Potapov, Appl. Phys. Lett. **107**, 072110 (2015).

[104] K. Muraki, S. Fukatsu, Y. Shiraki, and R. Ito, Appl. Phys. Lett. **61**, 557 (1992).

[105] B. Voigtländer and A. Zinner, Appl. Phys. Lett. **63**, 3055 (1993).

[106] D. J. Eaglesham, F. C. Unterwald, and D. C. Jacobson, Phys. Rev. Lett. **70**, 966 (1993).

[107] J. Falta, Th. Schmidt, G. Materlik, J. Zeysing, G. Falkenberg, and R. L. Johnson, Appl. Surf. Sci. **162-163**, 256 (2000).